JOURNAL OF GEOPHYSICAL RESEARCH, VOL. 112, B02401, doi:10.1029/2005JB004210, 2007

Seismic structure of the Endeavour Segment, Juan de Fuca Ridge: Correlations with seismicity and hydrothermal activity

E. M. Van Ark,[1] R. S. Detrick,[2] J. P. Canales,[2] S. M. Carbotte,[3]
A. J. Harding,[4] G. M. Kent,[4] M. R. Nedimovic,[3] W. S. D. Wilcock,[5]
J. B. Diebold,[3] and J. M. Babcock[4]

Received 9 December 2005; revised 23 June 2006; accepted 21 September 2006; published 3 February 2007.

[1] Multichannel seismic reflection data collected in July 2002 at the Endeavour Segment, Juan de Fuca Ridge, show a midcrustal reflector underlying all of the known high-temperature hydrothermal vent fields in this area. On the basis of the character and geometry of this reflection, its similarity to events at other spreading centers, and its polarity, we identify this as a reflection from one or more crustal magma bodies rather than from a hydrothermal cracking front interface. The Endeavour magma chamber reflector is found under the central, topographically shallow section of the segment at two-way traveltime (TWTT) values of 0.9–1.4 s (∼2.1–3.3 km) below the seafloor. It extends approximately 24 km along axis and is shallowest beneath the center of the segment and deepens toward the segment ends. On cross-axis lines the axial magma chamber (AMC) reflector is only 0.4–1.2 km wide and appears to dip 8–36° to the east. While a magma chamber underlies all known Endeavour high-temperature hydrothermal vent fields, AMC depth is not a dominant factor in determining vent fluid properties. The stacked and migrated seismic lines also show a strong layer 2a event at TWTT values of 0.30 ± 0.09 s (380 ± 120 m) below the seafloor on the along-axis line and 0.38 ± 0.09 s (500 ± 110 m) on the cross-axis lines. A weak Moho reflection is observed in a few locations at TWTT values of 1.9–2.4 s below the seafloor. By projecting hypocenters of well-located microseismicity in this region onto the seismic sections, we find that most axial earthquakes are concentrated just above the magma chamber and distributed diffusely within this zone, indicating thermal-related cracking. The presence of a partially molten crustal magma chamber argues against prior hypotheses that hydrothermal heat extraction at this intermediate spreading ridge is primarily driven by propagation of a cracking front down into a frozen magma chamber and indicates that magmatic heat plays a significant role in the hydrothermal system. Morphological and hydrothermal differences between the intermediate spreading Endeavour and fast spreading ridges are attributable to the greater depth of the Endeavour AMC and the corresponding possibility of axial faulting.

Citation: Van Ark, E. M., R. S. Detrick, J. P. Canales, S. M. Carbotte, A. J. Harding, G. M. Kent, M. R. Nedimovic, W. S. D. Wilcock, J. B. Diebold, and J. M. Babcock (2007), Seismic structure of the Endeavour Segment, Juan de Fuca Ridge: Correlations with seismicity and hydrothermal activity, *J. Geophys. Res.*, *112*, B02401, doi:10.1029/2005JB004210.

1. Introduction

[2] Morphological and hydrothermal differences between fast spreading and slow spreading mid-ocean ridge systems have led to the hypothesis that these systems have fundamentally different mechanisms of heat extraction and hydrothermal circulation [*Lister*, 1974, 1980a, 1980b, 1982; *Fornari and Embley*, 1995; *Wilcock and Delaney*, 1996]. The permeability structure of the crust and subsequent hydrothermal venting at fast spreading ridges is thought to be controlled by diking events from a steady state axial magma chamber (Figure 1a). This results in small, relatively short-lived hydrothermal vents whose heat flux increases

---

[1] MIT-WHOI Joint Program, Woods Hole Oceanographic Institution, Woods Hole, Massachusetts, USA.

[2] Department of Marine Geology and Geophysics, Woods Hole Oceanographic Institution, Woods Hole, Massachusetts, USA.

[3] Division of Marine Geology and Geophysics, Lamont-Doherty Earth Observatory, Columbia University, Palisades, New York, USA.

[4] Institute of Geophysics and Planetary Physics, Scripps Institute of Oceanography, University of California, San Diego, La Jolla, California, USA.

[5] School of Oceanography, University of Washington, Seattle, Washington, USA.

0148-0227/07/2005JB004210$09.00

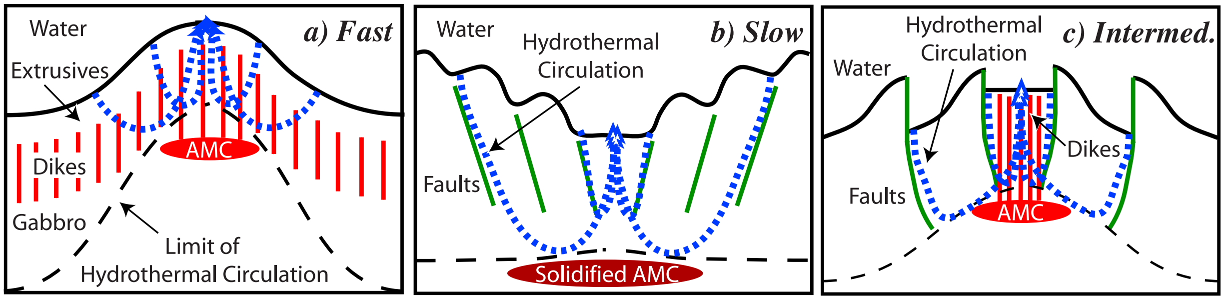

Figure 1. Cartoons illustrating proposed hydrothermal circulation regimes for fast, slow, and intermediate spreading centers. Thick dotted lines show proposed paths of hydrothermal circulation through the crust. (a) Fast spreading ridges may have hydrothermal circulation controlled by the heat and porosity provided by an axial magma chamber (AMC) with frequent diking and eruptive events. Hydrothermal vents are relatively short-lived and major faults are absent in the axial region [*Wilcock and Delaney*, 1996]. (b) Slow spreading ridges, in contrast, may have circulation controlled by faulting and heat mining through propagation of a cracking front into a frozen magma chamber. Hydrothermal systems can be long-lived and are often localized along major faults [*Wilcock and Delaney*, 1996]. (c) Intermediate spreading ridges appear to include elements of both faster spreading ridges (a midcrustal magma body) and slower spreading ridges (long-lived, fault-controlled hydrothermal systems). Faulting along the margins of the neovolcanic zone may be controlled by episodic dike intrusion as opposed to lithospheric extension as at slow spreading ridges [*Carbotte et al.*, 2006].

following magmatic eruptions, as observed at the fast spreading East Pacific Rise (EPR) [*Haymon et al.*, 1991, 1993; *Baker et al.*, 2002]. In contrast, control of the permeability structure of crust at slow spreading ridges has been attributed to extension-driven faulting and downward propagation of a cracking front into the lower crust where either no magma chamber is present or small, deep, pockets of melt occur (Figure 1b). This can lead to long-lived hydrothermal systems and massive sulfide deposits whose activity does not seem to be consistently correlated with recent volcanism, exemplified by the TAG hydrothermal system on the slow spreading Mid-Atlantic Ridge (MAR) [*Wilcock and Delaney*, 1996; *White et al.*, 1998].

[3] The Juan de Fuca Ridge (5.6–5.7 cm/yr full spreading rate [*Wilson*, 1993; *DeMets et al.*, 1994]) is often taken as the type example of intermediate spreading rate mid-ocean ridges (4–9 cm/yr full spreading rate). Previous studies of the morphology and hydrothermal vent structures of the Juan de Fuca Ridge (Figure 2) led to the hypothesis that the Endeavour Segment was an example of the slow spreading ridge style of heat extraction, controlled by the downward propagation of a cracking front into a frozen magma chamber [*Wilcock and Delaney*, 1996; *Kelley et al.*, 2002]. The Endeavour Segment has a ~150 m deep axial valley with numerous faults and fissures and there is no evidence of recent eruptions (although preliminary U series dating of recently collected lavas indicates ages of several thousand years (J. Gill, personal communication, 2005)). This suggested that Endeavour is currently in an extension-dominated tectonic regime rather than a magmatic regime [*Delaney et al.*, 1992; *Kappel and Ryan*, 1986; *Tivey and Delaney*, 1986]. The large size, regular spacing, and location of known Endeavour high-temperature vent fields along visible faults and fissures in the axial valley floor suggested a long-term pattern of stable subsurface hydrothermal circulation consistent with a cracking front model of heat extraction [*Tivey and Delaney*, 1986; *Delaney et al.*, 1992; *Robigou et al.*, 1993; *Butterfield et al.*, 1994; *Lilley et al.*, 1995; *Wilcock and Delaney*, 1996; *Delaney et al.*, 1997; *Yoerger et al.*, 2000; *Kelley et al.*, 2001, 2002, 2003]. In addition, the large heat fluxes recorded at the Endeavour hydrothermal vent fields were thought to be high enough to freeze a magma chamber with a thin conductive lid [*Lister*, 1974, 1980a, 1980b, 1982; *Wilcock and Delaney*, 1996].

[4] Evidence from petrology and seismology was also interpreted as supporting the cracking front model at Endeavour. Lavas collected from the Endeavour axial valley have enriched and transitional mid-ocean ridge basalt (EMORB and TMORB) signatures and a high degree of heterogeneity over short-length scales which suggests a low degree of melting in a clinopyroxene-rich source [*Karsten et al.*, 1990; *Sours-Page et al.*, 1999]. Levels of seismicity on the Endeavour Segment [*Wilcock et al.*, 2002] were much higher than observed at the EPR [*Sohn et al.*, 1998, 1999] in similar ocean bottom seismometer experiments conducted in 1995. At the EPR axial seismicity is confined to the uppermost 1 km of crust [*Sohn et al.*, 1998, 1999] while at Endeavour seismicity in the axial region occurs in a depth range of 1.5–3.5 km [*Wilcock et al.*, 2002]. The predominant focal mechanism for both EPR and Endeavour microearthquakes implies a thermal cracking source; however, the EPR hypocenters are located at least 300 m above the axial magma chamber (AMC) reflection imaged by *Kent et al.* [1993a] while the Endeavour hypocenters were thought to extend to depths greater than the apparent depth of the one possible AMC reflection imaged prior to this work [*Rohr et al.*, 1988]. Finally, the SEISRIDG-85 seismic refraction survey [*Cudrak et al.*, 1987; *Cudrak*, 1988; *White and Clowes*, 1990; *Cudrak and Clowes*, 1993] failed to find major low-velocity anomalies under the Endeavour axial high, as would be expected for an active magmatic system.

[5] Here we present data from a July 2002 multichannel seismic reflection survey of the Juan de Fuca Ridge on the R/V *Maurice Ewing* [*Carbotte et al.*, 2006] which shows that all of the major Endeavour Segment hydrothermal vent fields are underlain by a crustal magma chamber at a depth

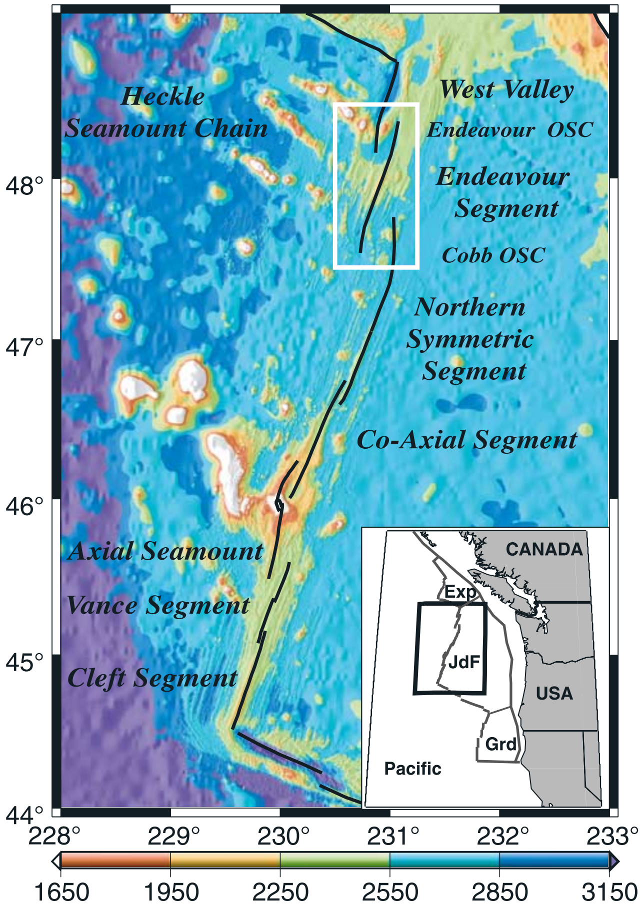

Figure 2. Bathymetry of the Juan de Fuca Ridge (in meters) showing the location of the Endeavour segment (white box outlines location of Figure 3) and the plate boundary (black line). The Endeavour Segment is bounded to the north by the Endeavour overlapping spreading center (OSC) and to the south by the Cobb OSC. Inset shows tectonic setting of the Juan de Fuca Ridge, where JdF, Juan de Fuca Plate; Exp, Explorer Plate; Grd, Gorda Plate; and Pacific, Pacific Plate (black box outlines location of main map).

of ~2.1–3.3 km below the seafloor. Earthquake hypocenters in the axial region occur just above this magma body. We therefore conclude that the heat extraction mechanism at intermediate spreading systems such as the Endeavour Segment requires a model distinct from that of both fast and slow spreading ridges. One proposed intermediate heat extraction model (Figure 1c) features a magmatic heat source with hydrothermal circulation pathways determined by dike-controlled faulting along the margins of the neovolcanic zone [*Carbotte et al.*, 2006]. The magmatic hydrothermal system at intermediate spreading ridges thus appears to include elements of both faster spreading ridges (a midcrustal magma body) and slower spreading ridges (long-lived, fault-controlled hydrothermal systems).

2. Overview of the Endeavour Segment

2.1. Morphology and Geology

[6] The Juan de Fuca Ridge (Figure 2) is the spreading boundary between the Pacific and Juan de Fuca plates. The ~90-km long Endeavour Segment is located between the Endeavour and Cobb overlapping spreading centers on the northern Juan de Fuca Ridge. The central portion of the Endeavour Segment out to crustal ages of ~500,000 years (Figure 3) is dominated by a series of ridge-parallel (orientation N20E) abyssal hills spaced ~6 km (~200,000 years) apart with intervening extensional basins. This ridge-basin pattern is superimposed on a broader (30–40 km wide) cross-axis swell of young oceanic crust [*Kappel and Ryan*, 1986; *Holmes and Johnson*, 1993]. The abyssal hills are asymmetric with outer constructional volcanic surfaces and inner steep faulted faces [*Kappel and Ryan*, 1986; *Tivey and Johnson*, 1987; *Holmes and Johnson*, 1993; *Delaney et al.*, 1997], a shape repeated in the current axial high (Figure 4). Sediment thicknesses on terrain younger than 0.8 Ma vary between a few meters and several tens of meters [*Holmes and Johnson*, 1993].

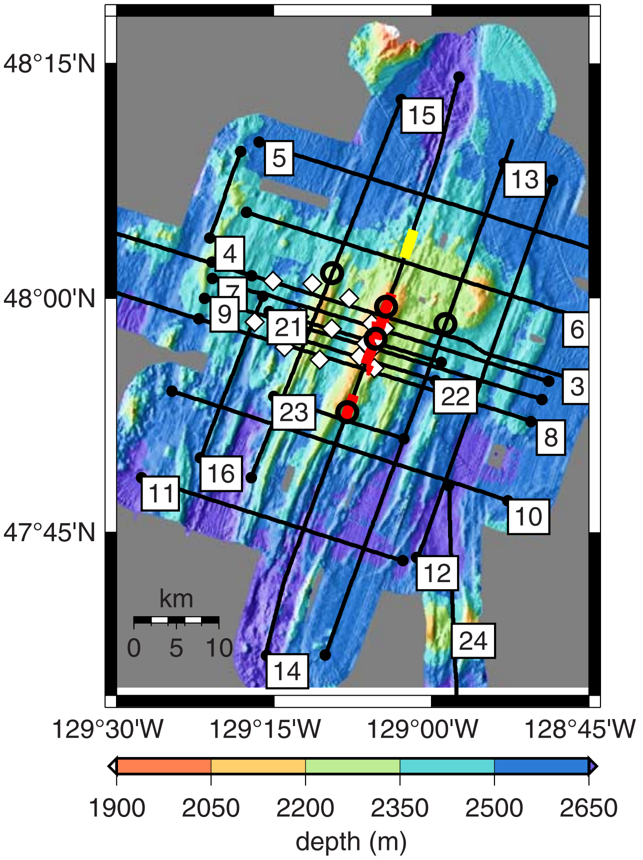

Figure 3. Bathymetry of the Endeavour Segment collected during the EW0207 seismic survey. Tracks of the seismic lines collected are labeled and shown using solid black lines. Red and yellow areas on Line 14 show axial magma chamber locations picked from the line 14 stack; red are more certain picks, and yellow are less certain picks. Black circles indicate locations of supergathers used to produce Figures 11 and 12. White diamonds show the locations of the ocean bottom seismometers used by *Wilcock et al.* [2002]. The location of the multichannel seismic reflection line shot by *Rohr et al.* [1988], as reported by *White and Clowes* [1990], is nearly coincident with our line 3.

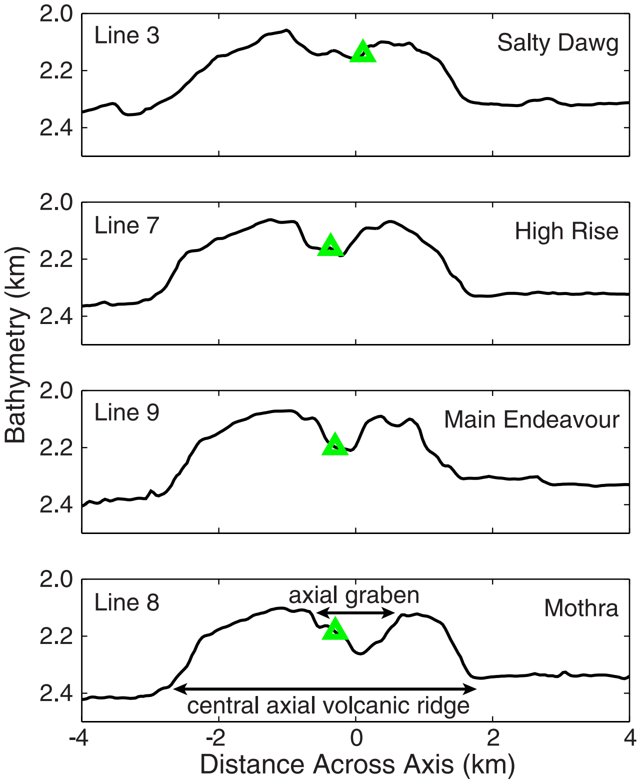

Figure 4. Bathymetry profiles across the Endeavour axial high at four vent field locations. Profiles follow the tracks of the labeled seismic lines and are centered at their intersection with the along-axis seismic line. Triangles show locations of indicated vent fields.

[7] The 25-km-long, 4-km-wide, and 300-m-high central axial volcanic ridge is rifted with a 0.8- to 1.4-km-wide axial graben (Figures 4 and 5). This axial graben deepens from north to south with 55–85 m relief at the latitude of the Salty Dawg vent field and 140–160 m relief at the latitude of the Mothra vent field (Figure 4) and is bounded by steep, inward facing normal fault surfaces [*Karsten et al.*, 1986; *Tivey and Delaney*, 1986]. SeaMARC I sonar imagery of the shoulders of the ridge crest suggested overlapping asymmetrical bulbous lava flows dripping down the outer sides of the ridge and identified intense faulting and fissuring confined to the axial graben [*Kappel and Ryan*, 1986]. Alvin submersible and DSL120 deep-towed side-scan sonar observations confirmed that the youngest volcanic units in the axial valley are truncated by recent faulting [*Tivey and Delaney*, 1986; *Delaney et al.*, 1992; *Bhat et al.*, 1997].

[8] These morphological details, combined with observations from other segments of the Juan de Fuca Ridge, were interpreted by *Kappel and Ryan* [1986] as supporting a model of episodic, volcanic construction with stages of ridge growth, summit trough collapse, and amagmatic axial extension and faulting, followed by renewed axial ridge growth. However, *Karsten et al.* [1986] noted that the shallowest portion of the Endeavour Ridge coincides with a broad plateau which marks the intersection of the Heckle Seamount chain with the ridge axis (Figure 2), suggesting long-term enhanced magma supply to that portion of the spreading axis. They also suggested that the north and south valleys located at either end of the Endeavour Ridge could be caused by diminished magma supply as magma flows along-axis from a central magma chamber under the shallowest portion of the ridge, in combination with the cooling effects due to thermal contrasts at the overlapping spreading centers at either end of the Endeavour Segment. More recently, *Carbotte et al.* [2006] have suggested that the periodic changes in seafloor relief moving away from the axis of the various Juan de Fuca Ridge segments could be attributed to variations in faulting controlled by magmatic, dike injection processes rather than the alternating tectonic-magmatic phases proposed by *Kappel and Ryan* [1986].

2.2. Hydrothermal Activity

[9] Hydrothermal vent fields on the Endeavour Ridge have been identified through seafloor mapping, water column thermal and chemical anomalies, dredging, and submersible observations and sampling [*Tivey and Delaney*, 1986; *Kadko et al.*, 1990; *Delaney et al.*, 1992; *Thomson et al.*,

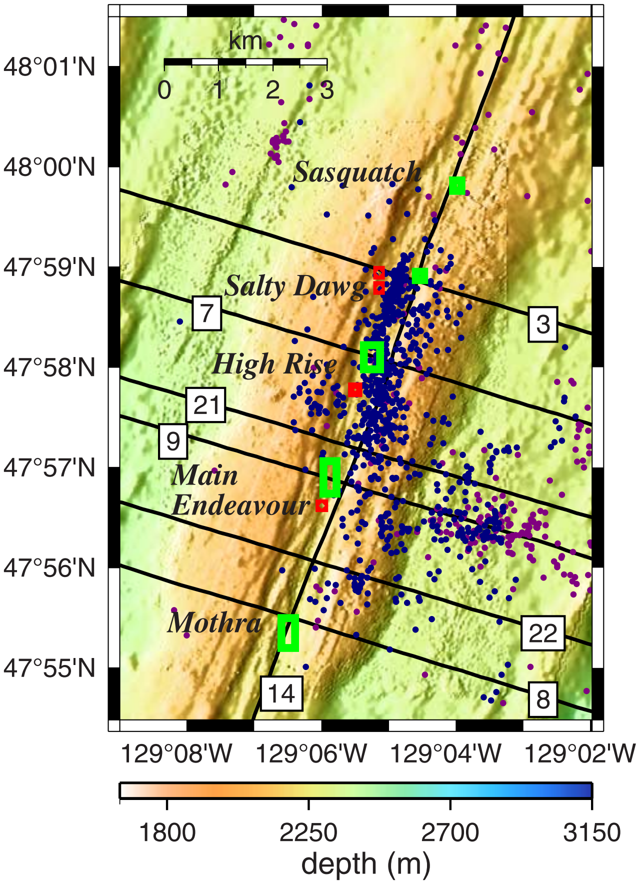

Figure 5. Bathymetry of the Endeavour Segment axial high. Green boxes show the location of the five known large, high-temperature hydrothermal vent fields. Red boxes show the location of diffuse, low-temperature vent fields: Cirque, Dune, Clambed, and Quebec, from north to south (vent locations from D. Glickson (personal communication, 2005)). Blue circles show microseismicity hypocenters located in latitude, longitude, and depth, while purple circles show hypocenters located only in latitude and longitude [*Wilcock et al.*, 2002].

1992; *Robigou et al.*, 1993; *Lilley et al.*, 1995; *Bhat et al.*, 1997; *Kelley et al.*, 2001]. Currently five large, high-temperature (300–400°C) vent fields have been identified [*Kelley et al.*, 2002], from north to south: Sasquatch [*Kelley et al.*, 2003], Salty Dawg [*Lilley et al.*, 1995], High Rise [*Robigou et al.*, 1993], Main Endeavour [*Tivey and Delaney*, 1986; *Delaney et al.*, 1992] and Mothra [*Kelley et al.*, 2001] (Figure 5). These high-temperature vent fields are on the order of 400–500 m long and are spaced approximately every 2–3 km along axis. All appear to be localized along major faults. Each vent field contains many tall (>20 m high) sulfide structures on top of which many smaller black smoker chimneys are found [*Tivey and Delaney*, 1986; *Delaney et al.*, 1992; *Robigou et al.*, 1993; *Kelley et al.*, 2001, 2002]. Diverse biological communities containing tube worms, sulfide worms, palm worms, galatheid crabs, and a variety of snails and limpets are sustained by lower temperature fluids venting through porous chimney walls and sulfide structure flanges found on the vents [*Sarrazin et al.*, 1997; *Kelley et al.*, 2002].

[10] Areas of diffuse, lower-temperature flow are present along-axis between these high-temperature vent fields (Figure 5), suggesting nested subsurface circulation cells [*Alt*, 1995; *Delaney et al.*, 1997; *Kelley et al.*, 2002]. Magnetic anomalies give further evidence for the isolation of deep, high-temperature circulation from shallower low-temperature circulation. High- resolution magnetic field data collected over the Endeavour axial valley reveal circular magnetization anomaly lows associated with known active and extinct hydrothermal vent complexes [*Tivey and Johnson*, 2002]. These circular anomalies were interpreted by *Tivey and Johnson* [2002] as the result of pipe-like zones of upward hydrothermal fluid flow under each vent system, each isolated through at least the magnetic layer (the top ~500 m of the crust) due to “armoring” by silica deposition [*Cann and Strens*, 1989; *Hannington et al.*, 1995; *Tivey et al.*, 1999].

[11] Off-axis heat flow measurements 3–24 km perpendicular to the Endeavour Ridge [*Johnson et al.*, 1993] imply that crust younger than 1 Ma continues to cool primarily by circulation of hydrothermal fluid in topographically controlled pathways associated with deep crustal faults.

2.3. Microseismicity

[12] Ocean bottom seismometer (OBS) deployments on the Endeavour Ridge have detected abundant small-magnitude “microearthquakes” which seem to be associated with activity underneath the hydrothermal vent fields [*McClain et al.*, 1993; *Wilcock et al.*, 2002, 2004]. Earthquakes beneath the ridge axis are concentrated in a band of intense seismicity at 1.5–3.5 km depth with fault mechanisms showing subhorizontal tension axes oriented in all directions except parallel to the ridge, indicating a stress field influenced by both ridge spreading and hydrothermal cracking [*Wilcock et al.*, 2002]. Figure 5 shows the microseismicity observed in a 55-day OBS deployment in 1995 [*Wilcock et al.*, 2002]. More recent observations show a sharp drop in microseismic activity to the north of the High Rise vent field, which seems to correlate with a reduced vigor of hydrothermal venting [*Wilcock et al.*, 2004].

[13] Endeavour axial microearthquakes often occur in swarms, probably signaling either tectonic crustal-cracking events or magmatic diking events [*McClain et al.*, 1993; *Wilcock et al.*, 2002]. Correlations between microseismicity and black smoker visual activity, black smoker fluid temperature variations, and diffuse flow flux variations were first recorded by *Delaney et al.* [1990]. More recently, *Johnson et al.* [2000] reported on a 8 June 1999 earthquake swarm which was interpreted to be of tectonic origin and observed to correlate with vent temperature and inferred fluid flux increases. However, *Lilley et al.* [2003] presented evidence that chemical signatures in the vent fluids instead suggested a volcanic origin of the same microseismic swarm and *Bohnenstiehl et al.* [2004] interpreted hydroacoustic records of seismic swarms at Endeavour from March 1999 through January 2000 in terms of dike propagation.

2.4. Seismic Structure

[14] The only previous multichannel seismic reflection study of the Endeavour Ridge consisted of a single-cross axis line near the Main Endeavour vent field [*Rohr et al.*, 1988]. This profile revealed a narrow (~1 km wide) midcrustal axial reflector at a two-way traveltime (TWTT) of ~1.0 s, which was estimated to be 2.5 km below the seafloor. Since the low signal-to-noise of these data prevented determination of the polarity of the reflection and available refraction data [*Cudrak et al.*, 1987] did not indicate major velocity anomalies under the axis, *Rohr et al.* [1988] interpreted this reflector as an increase in seismic velocity related to a vertical thermal gradient caused by a hydrothermal circulation boundary.

[15] Seismic refraction data collected on the SEISRIDG-85 survey of the Endeavour segment [*Cudrak et al.*, 1987; *Cudrak*, 1988; *White and Clowes*, 1990; *Cudrak and Clowes*, 1993] also failed to find evidence for an axial magma chamber. Two-dimensional (2-D) traveltime tomography [*White and Clowes*, 1990] on a cross-axis line coincident with the reflection line of *Rohr et al.* [1988] was interpreted with a three layer upper crustal model with an abrupt velocity increase from 2.5 to 4.8 km/s 250–600 m below the seafloor attributed to a metamorphic front in pillow basalts. A shallow low-velocity anomaly with magnitude <~0.45 km/s beneath the ridge was attributed to a zone of hydrothermal circulation. No evidence was found for a crustal magma chamber at 1.5–3.5 km depth below seafloor; however, the sensitivity of the experiment required a zone of partial melt of at least 1 km width and 1 km thickness to produce a detectable delay in traveltime arrivals for rays passing through or around the body. Two-dimensional velocity models of the crust [*Cudrak and Clowes*, 1993] revealed significant lateral variations in thickness and velocity of crustal layers 2a, 2b, and 2c which appeared to be random rather than distributed symmetrically about the ridge. These variations were attributed to variations in fracturing, hydrothermal circulation, and magmatic and/or deformational processes. Again no evidence for a large crustal magma body was found, but a small (0.1–0.2 km/s) velocity decrease along axis in seismic layer 3 was interpreted as a possible indicator of elevated temperature.

3. Data Acquisition and Processing

[16] In a 30 day multichannel seismic (MCS) reflection survey of the Juan de Fuca Ridge on the R/V *Maurice*

Table 1. Data Processing Sequence and Parameters

Processing Step	Parameters
Geometry	
CMP gather	80-fold, 6.25 m CMP Interval
Trace Editing	
Hand-edit bad channels	
Automatic spike detection	0.5 s windows, 1.25–2.75 s TWTT on each trace
DMO-Based Suppression of Scattered Energy	
NMO	1500 m/s (water velocity)
Bottom mute below first multiple	
DMO f-k dip filter	apparent dips >2 ms/trace
Remove NMO	1500 m/s
Stacking	
Band-pass filter	5–30 Hz, 12 dB/octave
Velocity analysis	every 100 CMP
NMO mute	stretch and surgical
Stack	
Time Migration	
Band-pass filter	5–30 Hz, 12 dB/octave
Top mute above seafloor	
Finite difference algorithm[a]	maximum dip 5 ms/trace, layer thickness 50 ms
Display	
Band-pass filter	5–30 Hz, 12 dB/octave
Top mute above seafloor	
Bottom mute below first multiple	
AGC for stack plots	200 ms window
Exponential gain for migrated plots	24 db amplitude increase from 0–0.5 s below the seafloor

[a] Algorithm of *Lowenthal et al.* [1976].

Ewing in July 2002 [*Carbotte et al.*, 2002; *Detrick et al.*, 2002a], nine days were spent surveying the Endeavour segment (Figure 3). A total of 23 MCS lines were collected parallel and perpendicular to the ridge axis; each line was between 16.4 and 73.3 km long. The track lines were chosen so that 30- to 40-km-long cross-axis lines would be spaced 3–10 km apart and ridge-parallel lines would follow isochrons at 0.25 Ma (lines 15 and 13) and 0.5 Ma (lines 16 and 12) on both ridge flanks. Isochron lines were located along abyssal hills where possible to minimize side scattering from nearby shallow topography. Line 14 runs along the axis of the Endeavour Segment while lines 3, 7, 8, and 9 were positioned to cross the four vent fields known at the time of the cruise: Salty Dawg, High Rise, Mothra, and Main Endeavour, respectively.

[17] The MCS data for this study were collected using the R/V *Maurice Ewing*'s 6-km-long, 480-channel Syntron digital streamer with hydrophone group spacing of 12.5 m, maintained at a depth of ~7.5 m. The seismic source was a 3005 cubic inch air gun array, also towed at a nominal depth of 7.5 m, which fired every 37.5 m. For each shot, data were recorded for 10.24 s. A 4-ms sampling interval was used for lines focused on studying the ridge axis and a 2-ms sampling interval was used on the long, sediment-covered ridge flank lines which are presented elsewhere [*Nedimovic et al.*, 2005].

[18] Table 1 summarizes the processing sequence applied to the MCS data. Dip-moveout migration and dip filtering were performed on all cross-axis lines to eliminate side-scattered energy from seafloor topography [*Kent et al.*, 1996]. The axis-parallel lines were associated with smoother topography and less scattering, which made prestack dip filtering unnecessary for these lines. Although dip filtering was not applied to the along-axis lines, our interpretation is limited to events that are consistent between the cross and along-axis lines, so we are confident that those events are not out-of-plane noise. A poststack finite difference time migration was applied to all cross-axis lines using the 1-D crustal velocity function compiled by *Wilcock et al.* [2002] from earlier Endeavour reflection and refraction seismic experiments [*Rohr et al.*, 1988; *Cudrak and Clowes*, 1993] hung from the seafloor. We processed all of the Endeavour segment lines, but present only the most relevant subset in this paper.

4. Results

4.1. Along-Axis Seismic Structure

4.1.1. Layer 2a

[19] The stacked along-axis line 14 (Figure 6) shows a strong continuous event throughout the line at a two-way traveltimes (TWTT) of 140–500 ms below the seafloor. We interpret this event as marking the base of seismic layer 2a, which probably corresponds to the transition from volcanic extrusives above to predominantly dikes below (layer 2b) [*Harding et al.*, 1993]. The on-axis layer 2a is thin (140–270 ms TWTT) beneath the northern part of the Endeavour Ridge and then thickens systematically up to almost 500 ms TWTT south of the midsegment axial high (Figure 7, top). The 2a event can be traced all the way to the northern end of line 14 but disappears to the south of the midsegment axial high. The southern disappearance of the layer 2a event may be related to the overlap between the Endeavour Segment and the Northern Symmetric Segment at the Cobb Offset (Figure 2).

4.1.2. AMC

[20] The line 14 section (Figure 6) also shows a clear midcrustal reflection under the shallowest section of the spreading segment at two-way traveltimes of 0.9–1.4 s below the seafloor. This reflector is interpreted as the top of an axial magma chamber reflection based on its polarity

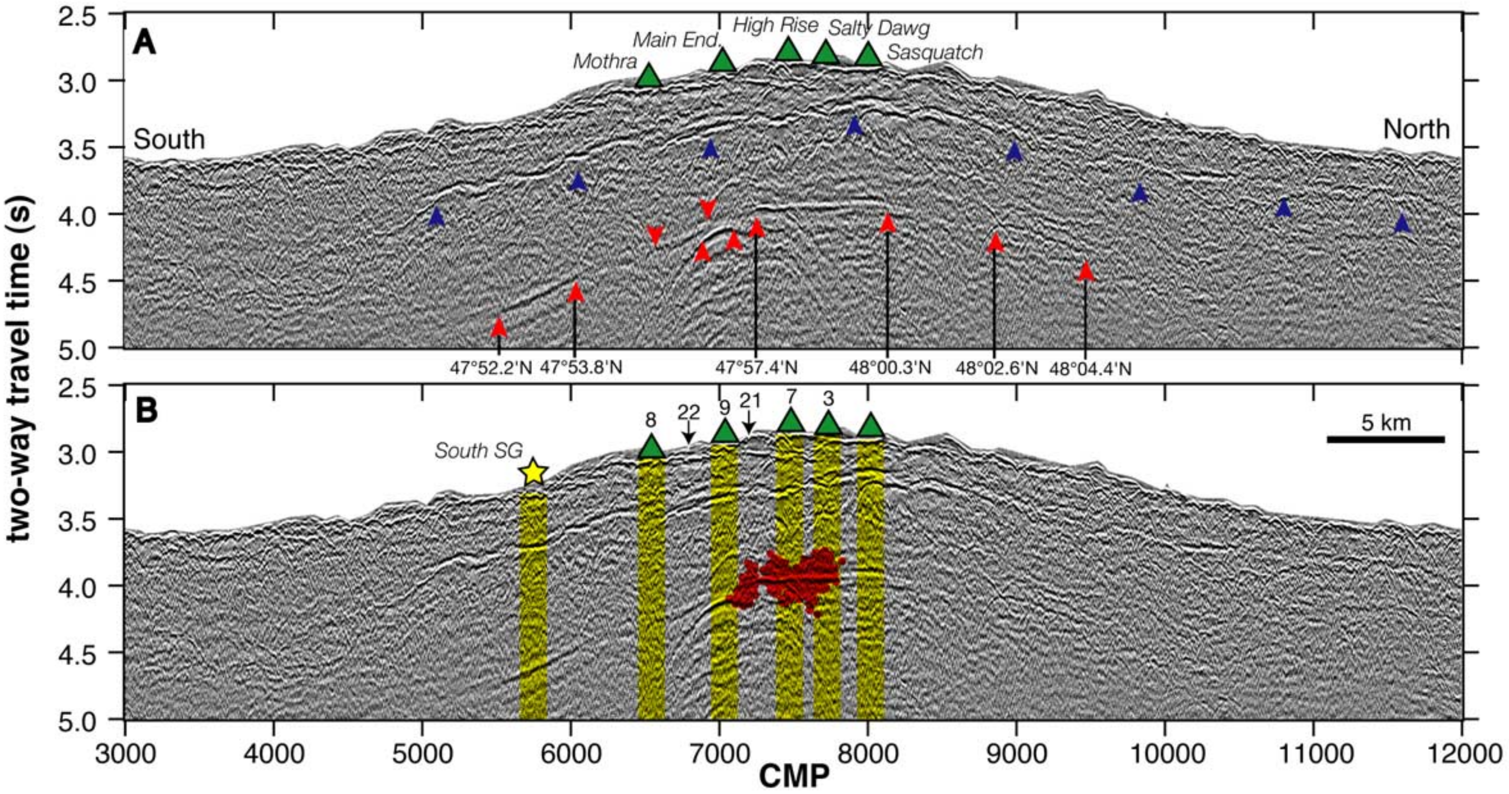

Figure 6. Figures 6a and 6b show the same stack of along-axis line 14. Green triangles show locations of the five large hydrothermal vent fields. (a) Blue arrows indicate the seismic layer 2a event and red arrows indicate the segments of the axial magma chamber reflection. Latitude labels show the extent of the southernmost, northernmost, and shallowest AMC segments. (b) Red circles show relatively relocated microseismicity hypocenters within 0.5 km of the line [*Wilcock et al.*, 2002]. Numbers label points where line 14 intersects cross-axis lines. Yellow star shows the location of the southern supergather. Yellow highlights indicate regions of the subsurface underlying known high-temperature hydrothermal vent fields and the southern supergather.

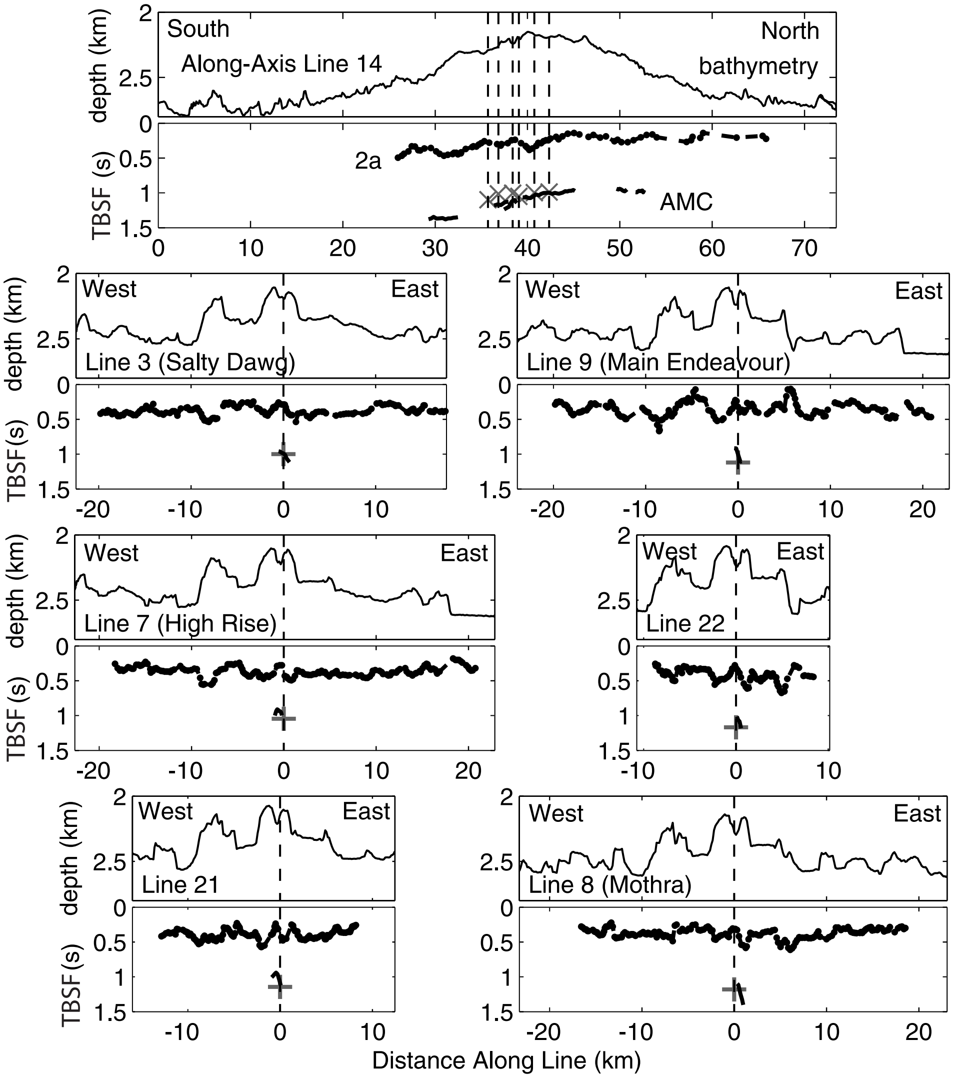

Figure 7. (top) Bathymetry and two-way traveltimes below the seafloor (TBSF) for 2a (upper black dots) and AMC picks (lower black dots) from stacked line 14 and migrated cross-axis seismic sections (Figures 6 and 10). Vertical dashed lines show the intersections of along and cross-axis lines. Gray cross marks on along-axis line 14 show the TBSF of AMC picks on cross-axis lines where they intersect with line 14 (from left to right, lines 8, 22, 9, 21, 7, and 3). Gray crosses show the TBSF of the AMC from line 14 where it intersects each cross axis line.

(presented below) and its similarity in geometry and reflection character to AMC reflections imaged and studied extensively along both the northern [*Kent et al.*, 1993a, 1993b; *Collier and Singh*, 1997, 1998; *Carbotte et al.*, 2000] and southern [*Kent et al.*, 1994; *Hooft et al.*, 1997] East Pacific Rise, along the Galapagos Spreading Center [*Detrick et al.*, 2002b; *Blacic et al.*, 2004], at the Valu Fa Ridge, Lau Spreading Center [*Collier and Sinha*, 1992; *Jacobs et al.*, 2003], and along the Southeast Indian Ridge [*Baran et al.*, 2005].

[21] The AMC reflector appears segmented into four or five sections, from south to north between CMPs 5500–6100 at two-way travel times (TWTTs) of 4.7–4.4 s, between CMPs 6600 and 6950 at TWTTs of 4.2–4.1 s, between CMPs 6900 and 7100 at TWTTs of 4.2–4.1 s, between CMPs 7100 and 8300 at a traveltime of 3.9–4.0 s, and a weak but possible AMC event between CMPs 8900 and 9500 at traveltimes of 4.1–4.3 s. The apparent overlap of the second and third events is likely an artifact of diffraction effects around the CMP 6900–7100 event. CMP gathers of data in the CMP 8900–9500 range show some subseafloor reflections, but they are often overwhelmed by scattered energy from the seafloor and our identification of the northernmost event as an AMC reflection is therefore tentative. This gives the axial magma chamber a total possible along-axis extent of 16–24 km, depending on whether the weak, northernmost event is included. The reflections seem more characteristic of a segmented series of magma lenses than a continuous magma body; however, this could be an artifact of streamer feathering [*Nedimovic et al.*, 2003], seafloor topography, or the inherent problems of imaging a narrow 3-D body with a single profile. The apparent length scale of

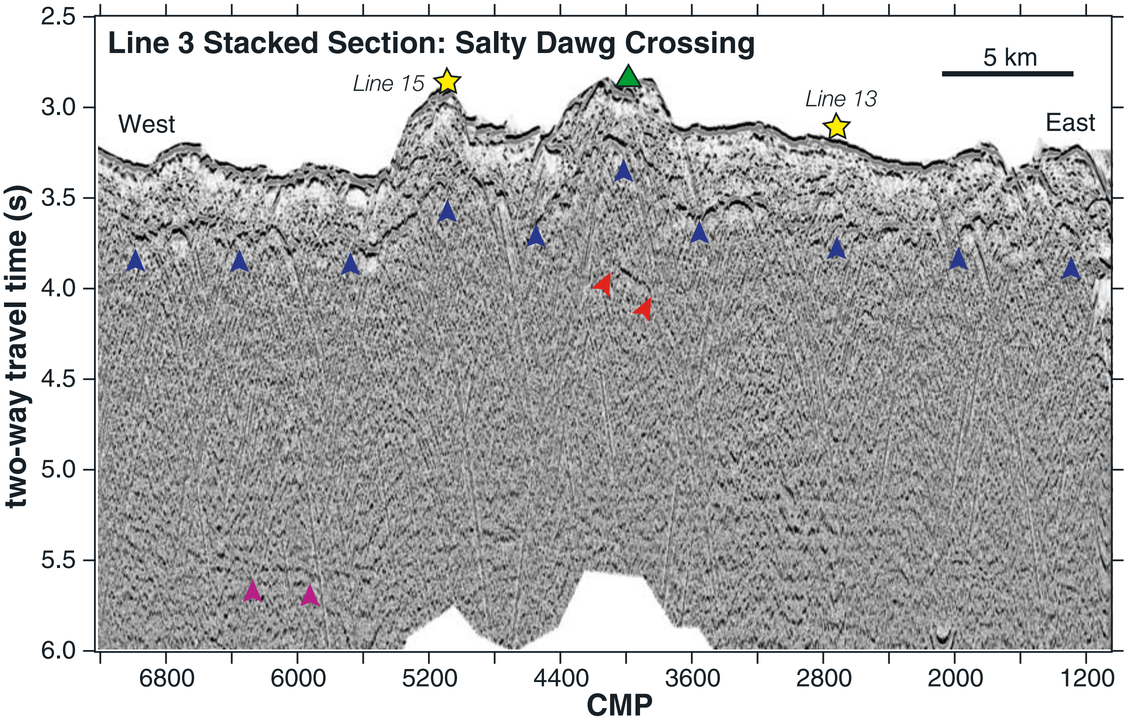

Figure 8. Stack of cross-axis line 3. Triangle shows the location of the Salty Dawg hydrothermal vent field. Stars shows where axis-parallel lines 13 and 15 cross line 3; the line 15 and line 13 supergathers are located to the northeast of these intersections (see Figure 3). Blue arrows indicate the seismic layer 2a event, red arrows at ~4.0 s TWTT indicate the AMC reflection, and magenta arrows at ~5.7 s TWTT indicate a probable Moho reflection.

the segmentation is consistent with that observed at other well-studied ridges [*Collier and Sinha*, 1992; *Kent et al.*, 1993a; *Hooft et al.*, 1997; *Carbotte et al.*, 2000; *Blacic et al.*, 2004; *Baran et al.*, 2005].

[22] The thickest axial layer 2a occurs above the deepest part of the AMC (Figures 6 and 7). This is consistent with the predicted positive correlation between AMC depth and 2a thickness due to the ability of a magma lens under higher pressure to push more magma to the surface [*Buck et al.*, 1997]. Such a correlation has also been observed at other ridges [e.g., *Blacic et al.*, 2004].

4.2. Cross-Axis Seismic Structure

[23] Figure 8 shows the full length of a single cross-axis stacked section (line 3), displaying the off-axis layer 2a variability and an example of weakly imaged Moho. Figure 9 shows the central portion of all the stacked sections which sample the Endeavour axial magma chamber (lines 3, 7, 21, 9, 22, and 8, from north to south), and Figure 10 shows the migrated versions of those same stacked sections. We present both the stacked and migrated sections because the AMC reflector is better imaged on the stacks while the layer 2a event is better imaged on the migrated sections. The migration process collapses diffractions from the edges of the magma chamber reflection but also introduces artifacts which make it more difficult to pick the subhorizontal AMC reflections. Seismic layer 2a events and AMC reflections are picked from the along and cross-axis lines and displayed along with bathymetry in Figure 7.

4.2.1. Layer 2a

[24] A strong, continuous seismic layer 2a event can be seen on the stacked (Figures 8 and 9) and migrated (Figure 10) seismic sections. Figure 7 shows that the mean layer 2a thickness perpendicular to the Endeavour Ridge is relatively constant with mean values for each line between 350 and 420 ms two-way travel time below the seafloor (TBSF) and standard deviations for each line ranging between 70 and 100 ms. These results are consistent with results of the seismic refraction study on the Endeavour Segment reported by *Cudrak and Clowes* [1993]. Visual inspection of Figure 7 shows some level of correlation between bathymetry and 2a thickness with thicker 2a sometimes occurring under the shallower bathymetry associated with the axis-parallel volcanic ridges. This is most clearly evident on lines 3, 7, and 9 where thicker 2a seems to occur under the volcanic ridge ~7–9 km to the west of the axis.

4.2.2. AMC

[25] The stacked and migrated cross-axis lines in Figures 8, 9, and 10 show midcrustal AMC reflections at two-way traveltimes consistent with those of the AMC on the along-axis line 14 (Figure 6). The cross-axis AMC reflections are narrow (0.5–1.2 km wide) and they tend to dip from shallower depths under the ridge axis to greater depths under the eastern flank of the ridge axis. Moving from north to south, the AMC events for lines 3, 7, 21, and 9 all appear at a range of two-way traveltimes between 0.9 and 1.1 s below the seafloor, while the AMC events are progressively deeper for line 22 (1.0–1.2 s TBSF) and line

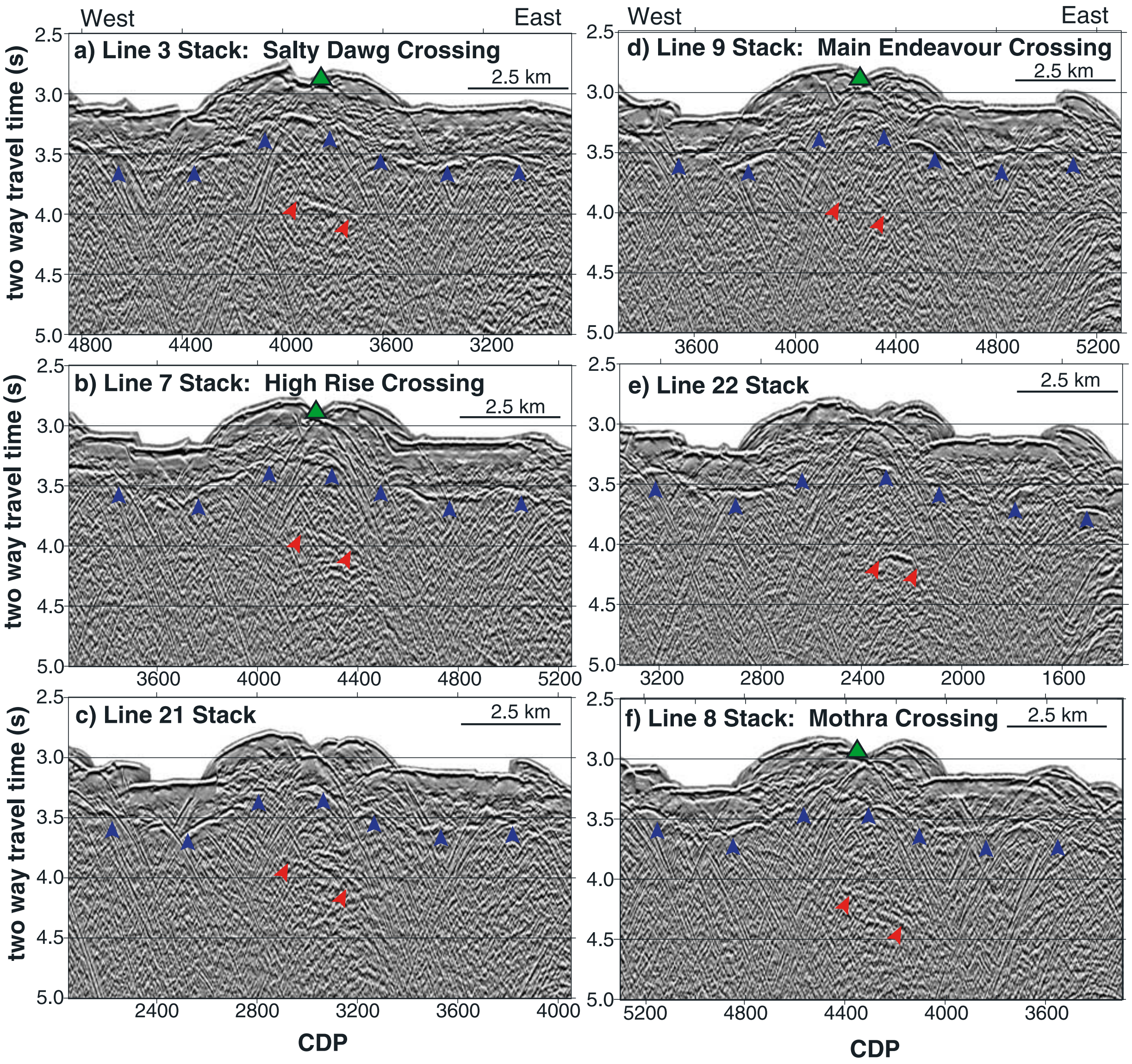

Figure 9. Stacks of cross-axis lines 3, 7, 21, 9, 22, and 8 (in order from north to south). Triangles show location of the hydrothermal vent fields. Blue arrows indicate the seismic layer 2a event, and red arrows indicate the AMC reflection.

8 (1.1–1.4 TBSF). This implies that magma chamber depths below the Salty Dawg, High Rise, and Main Endeavour vent fields are similar while the magma chamber beneath the Mothra vent field is significantly deeper, which is consistent with the AMC imaged on along-axis line 14 (Figure 6).

[26] The AMC event has the highest amplitudes on line 3, which crosses the Salty Dawg vent field, and line 22, which crosses the axis between the Main Endeavour and Mothra vent fields. The event is weaker on the other lines. It is probable that large lateral velocity changes due to rough seafloor topography for the cross-axis lines result in complex raypaths that cannot be modeled using the simple two-way traveltime reflection equation that was developed for at most gently dipping stratigraphy and smooth continuous interfaces. This would lead to poor and variable signal alignment (from CMP to CMP) before stack and variable signal strength (from CMP to CMP and from one line to another) of the AMC reflection on stacked sections. Furthermore, we show that the AMC is dipping east on all cross axis lines, which may have a significant impact on the strength of the AMC reflection. Prestack migrations or three-dimensional seismic studies may be required to better image the amplitude variability between the different cross-axis lines.

4.2.3. Moho

[27] A Moho reflection is weakly visible in a few locations on the cross-axis lines 3, 7, 8, and 9. One specific example is highlighted in Figure 8. In general, the Moho event appears at 2.0–2.3 s TWTT beneath the seafloor on the Endeavour cross-axis lines. This is consistent with the weak, very discontinuous, low-frequency Moho reflection event observed at 2.1–2.3 s TWTT at the Cleft Segment of the Juan de Fuca Ridge by *Canales et al.* [2005] and the

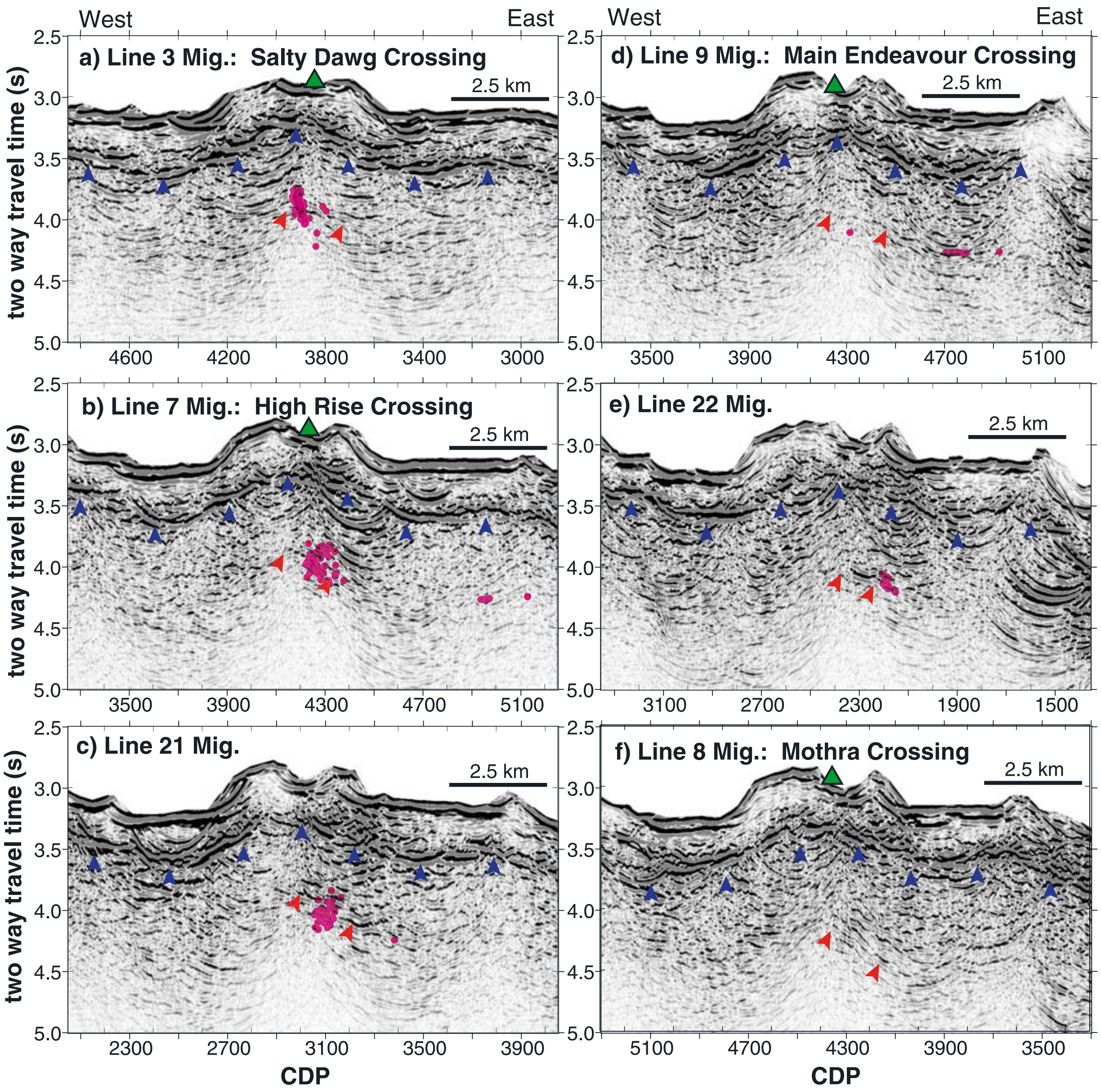

Figure 10. Migrations of cross-axis lines 3, 7, 21, 9, 22, and 8 (in order from north to south). Triangles shows location of the hydrothermal vent fields. Blue arrows indicate the seismic layer 2a event, and red arrows indicate the AMC reflection. Red circles show relatively relocated microseismicity hypocenters within 0.5 km of each line [*Wilcock et al.*, 2002].

Moho events observed by *Nedimovic et al.* [2005] for long cross-axis lines which sample the Juan de Fuca Ridge flanks.

4.3. Velocity Analysis

[28] To determine the Endeavour Segment upper crustal velocity structure we modeled the traveltimes of the main seismic arrivals observed in the data. One dimensional upper crustal velocities were forward modeled [*Zelt and Smith*, 1992] at three on-axis locations along line 14 and two off-axis locations (Figure 3). Two of the three on-axis locations were chosen to coincide with the Salty Dawg and Main Endeavour vent sites. The third was chosen at a location over the southern segment of the AMC in order to investigate possible differences between the main axial-high magma body and the deeper reflector to the south. The two off-axis locations were modeled using data from the axis-parallel lines 13 and 15 in order to minimize data complexity due to topographic effects. Both off-axis velocity analysis locations are positions close to the line 3 profile (Figure 8), one of the highest quality cross-axis profiles.

[29] To improve signal-to-noise ratios and to allow easier identification of the main seismic arrivals, fivefold constant-offset stacks (supergathers) were created at each location. For each supergather, the two-way traveltime of key arrivals were handpicked on all traces where they were visible (an example is shown in Figure 11). These events included the seafloor reflection, the retrograde refraction from the velocity transition at the base of layer 2a, and the refracted wave in

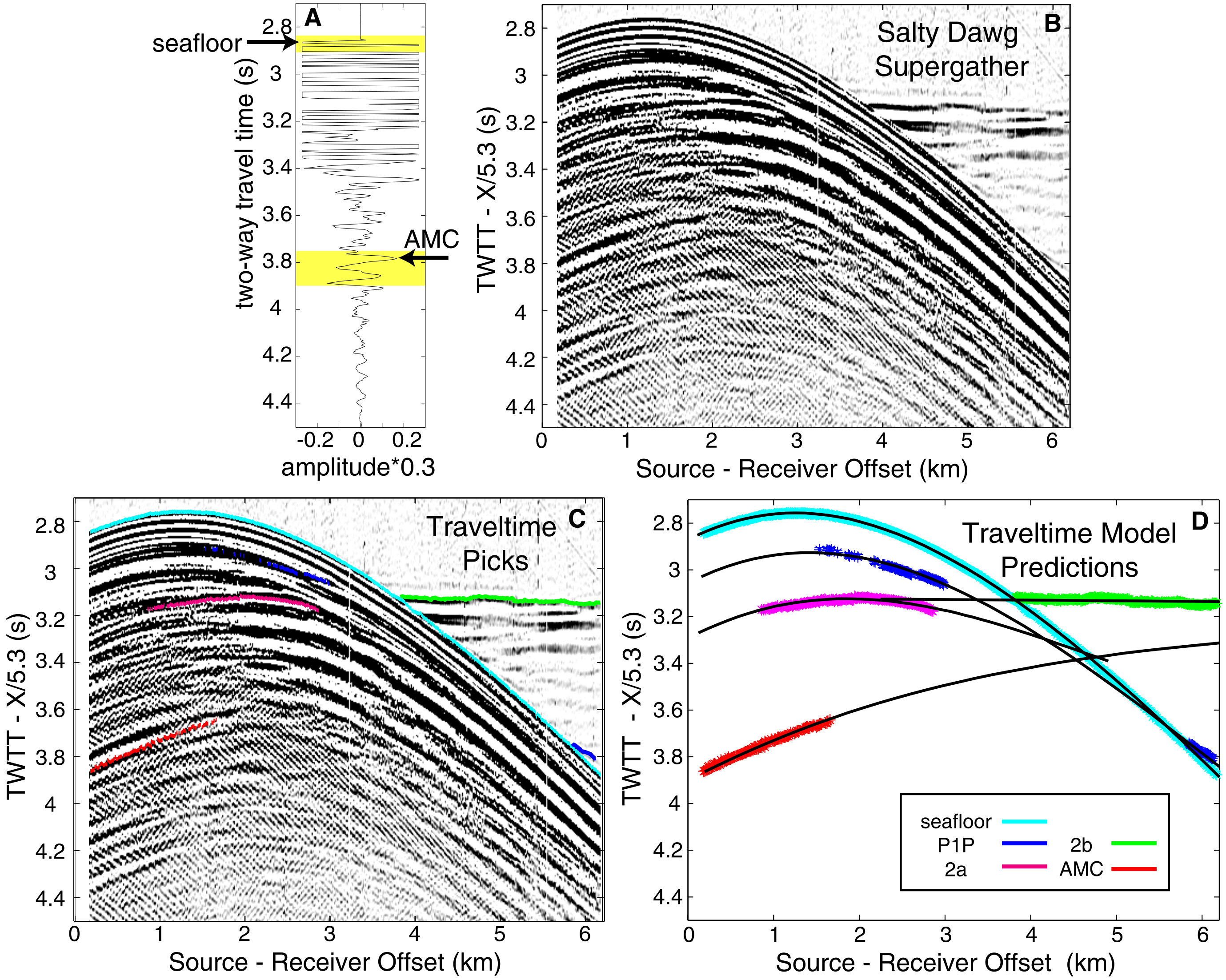

Figure 11. Salty Dawg supergather modeling and AMC polarity. (a) Trace created by stacking 0–1.5 km offset traces from the supergather shown in Figure 11b with normal moveout correction and without any filtering. Yellow boxes highlight the negative polarity of seafloor reflection and the opposite, positive polarity of the AMC reflection. The onset of the AMC event is indicated by the increase in amplitude and change in the frequency content of the signal. (b) Supergather of along-axis line 14 data with 30 CMPs located above the Salty Dawg vent field. (c) Same supergather overlain with the picks used to forward model the velocity structure of the upper crust at this location (same color code for events as in Figure 11d). (d) Supergather picks from Figure 11c with ±10 ms errors and traveltimes predicted from the one-dimensional Salty Dawg supergather velocity profile (black lines).

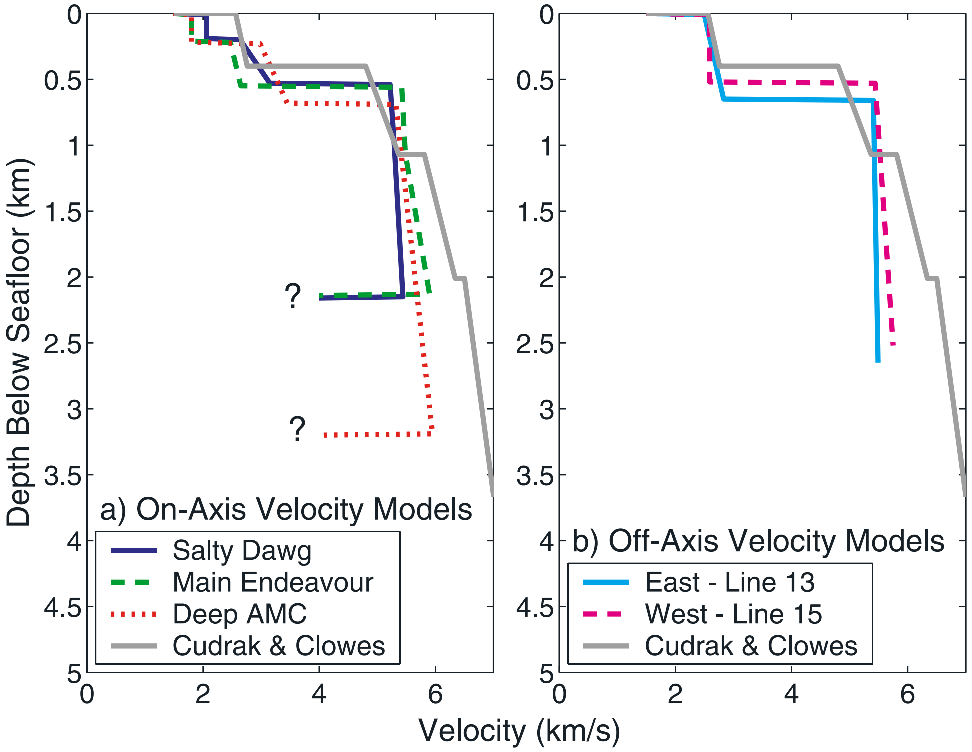

Figure 12. One-dimensional Endeavour velocity structures. (a) Blue, green, and red lines show velocity profiles derived from forward traveltime modeling of on-axis supergathers above two vent fields (Salty Dawg and Main Endeavour) and the southern, deep portion of the AMC. Velocities are only constrained by the supergather to the top of the AMC-associated negative velocity jump. Gray line shows the *Cudrak and Clowes* [1993] average one-dimensional Endeavour velocity structure for comparison. (b) Cyan and magenta lines show velocities from forward modeling of off-axis line 13 and 15 supergathers. The gray line again shows the *Cudrak and Clowes* [1993] velocity model for comparison.

seismic layer 2b on all supergathers. In addition, on the along-axis supergathers an intermediate event within layer 2a (labeled "P1P") and the reflection from the top of the midcrustal axial magma chamber reflector were identified and picked. The resulting velocity functions are shown in Figure 12.

[30] Layer 2a thicknesses in our velocity models are systematically greater (~200 m) than the thickness observed in the seismic reflection sections at the location of the velocity models, probably due to difficulty in picking the first arrival on the supergather sections. The layer 2a velocities of our off-axis velocity models (2.50–2.83 km/s) are comparable to those of the Cudrak and Clowes model (2.56–2.76 km/s). Uppermost layer 2a velocities of our on-axis models are significantly slower (1.80 km/s on Main Endeavour and the Deep AMC supergathers, 2.06 km/s under Salty Dawg) than the off-axis 2a velocities. However, the on-axis velocities at the bottom of layer 2a are somewhat faster (2.47–3.45 km/s) than those off-axis.

[31] The Salty Dawg, Main Endeavour, and Southern AMC supergather velocity functions have total seismic layer 2a thicknesses of 530, 550, and 680 meters, respectively. The line 13 and line 15 supergathers have total layer 2a thicknesses of 650 and 520 meters, respectively. The depth to the axial magma chamber is 2.1, 2.1, and 3.2 km below the seafloor on the Salty Dawg, Main Endeavour, and Deep AMC supergathers respectively. The thickness of the axial magma bodies and the velocity structure below the AMC in Figure 12a are unconstrained by the traveltime modeling, since we have no reflectors beneath the AMC to give us further information about the velocity structure at depth.

4.4. Variation of Layer 2a Thickness

[32] Two-way traveltimes for layer 2a observed on the reflection profiles were converted into depth using our velocity functions (Figure 12). Figure 13 shows that the thickness of crustal layer 2a varies between 180 and 630 m on the along-axis line 14. The mean ± standard deviation 2a thickness on all the cross-axis lines is 500 ± 110 m, and results for each line are presented in Table 2. Our results indicate that layer 2a thickness is highly variable without a clear pattern of off-axis thickening (Figure 14). This is unlike the Cleft and Vance segments of the southern Juan de Fuca Ridge [*Canales et al.*, 2005], the inflated portions of the Galapagos ridge [*Blacic et al.*, 2004], and the East Pacific Rise [*Harding et al.*, 1993] where the 2a thickness is seen to increase significantly off-axis.

[33] The range of layer 2a thicknesses measured on the Endeavour Segment lines presented here is 90–880 m. We report layer 2a thicknesses throughout this paper as mean ± standard deviations because the extremes of this range are more likely representative of either the effects of faulting or imaging issues associated with steep bathymetry and the

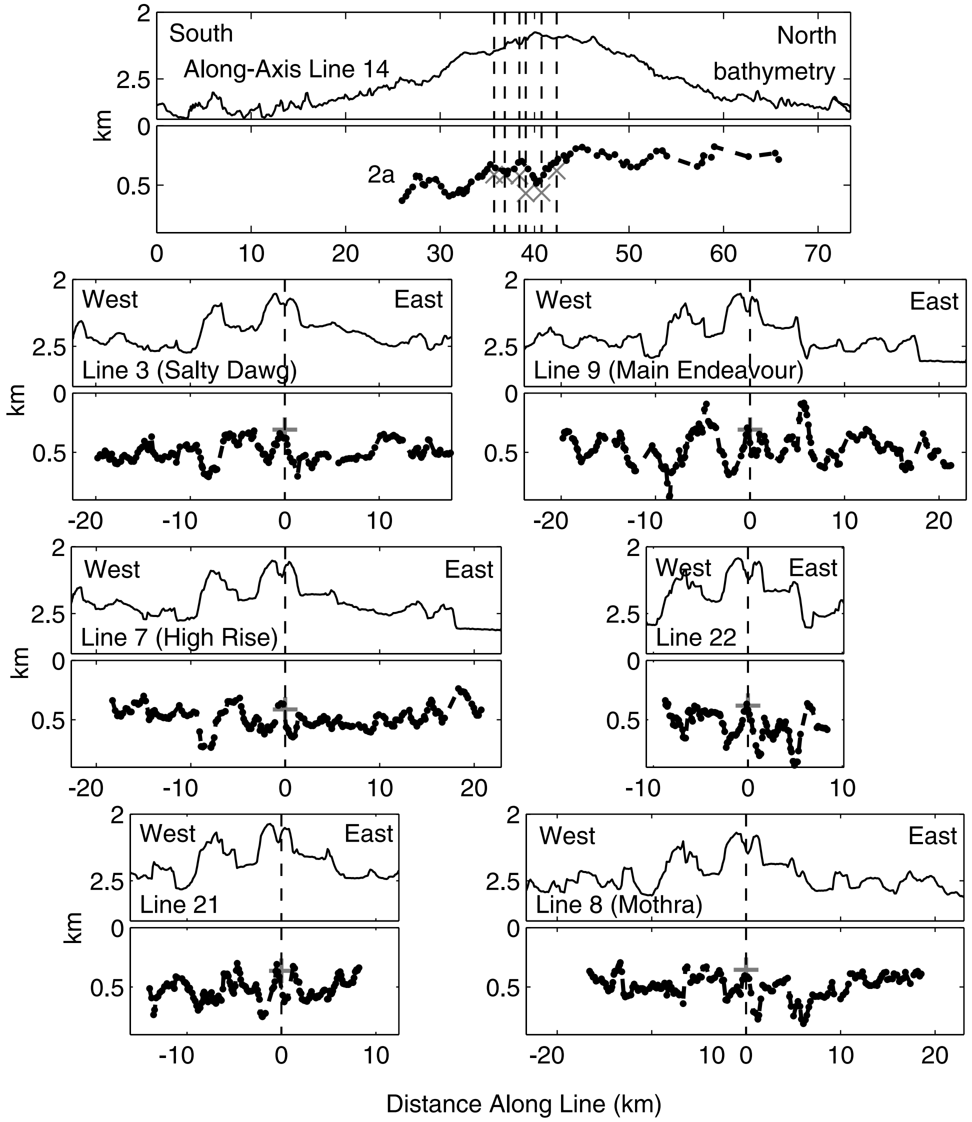

Figure 13. (top) Bathymetry (black line) and (bottom) layer 2a depths below the seafloor (black dots) from stacked line 14 and migrated cross-axis sections (Figures 6 and 10). Vertical dashed lines show the intersections of along and cross-axis lines. Gray cross marks on along-axis line 14 show the depth below the seafloor of layer 2a picks on cross-axis lines where they intersect with line 14 (from left to right, lines 8, 22, 9, 21, 7, and 3). Gray crosses show the depth below the seafloor of layer 2a from line 14 where it intersects each cross axis line. Picks were converted from two-way traveltime (TWTT) to depth using the on and off-axis average forward modeled supergather velocity functions Figure 12 as described in the text.

wide-angle nature of the 2a event than actual volcanic production of the ridge. This can be seen by examining Figure 13, especially the profile of line 9, where the extremes of 2a thickness are seen to occur underneath the faults bounding the off-axis volcanic ridges. While the means and standard deviations are more useful for trying to understand systematic variations between seismic lines, it is important to note that faulting is probably one of the factors which contributes to the large variability observed in Endeavour layer 2a thickness.

[34] In addition to the faulting contribution to layer 2a variability, the axis-parallel bathymetric highs often appear to be associated with a thicker layer 2a (Figures 13 and 14). This correlation between bathymetric highs and thicker layer 2a is consistent with the banded Endeavour upper crustal velocities observed by *Barclay and Wilcock* [2004] which show a correlation between slower velocities and bathymetric highs. The regions of thicker layer 2a and bathymetric highs could correspond to the intermittent periods of magma supply predicted by the model of *Kappel and Ryan* [1986]. Alternatively, these regions could correspond to the axial volcanic rift (AVR) building phase of the *Carbotte et al.* [2006] model, which assumes more steady state magma supply and predicts periodic topography through the interaction between dike-induced stress perturbations and tectonic extensional stresses.

Table 2. Summary of Layer 2a, AMC, and Moho Observations in Two-Way Traveltime Below the Seafloor and Depth Below the Seafloor[a]

	Layer 2a Thickness		Axial Magma Chamber			Moho
	TBSF, s	Depth, m	TBSF, s	Depth, km	Width, km	TBSF, s
Line 14 (along-axis)	0.30 ± 0.09	380 ± 120	0.9–1.4	2.2–3.3	16–24	
Line (Salty Dawg)3	0.39 ± 0.08	510 ± 100	1.0–1.1	2.2–2.4	1.2	2.0–2.2
Line 7 (High Rise)	0.37 ± 0.07	480 ± 90	0.9–1.0	2.1–2.3	0.8	2.1–2.4
Line 21	0.40 ± 0.07	520 ± 100	0.9–1.1	2.2–2.5	1.0	
Line 9 (Main Endeavour)	0.35 ± 0.11	460 ± 140	0.9–1.1	2.1–2.5	0.8	1.9–2.3
Line 22	0.42 ± 0.09	550 ± 120	1.0–1.2	2.3–2.6	0.4	
Line 8 (Mothra)	0.38 ± 0.07	490 ± 100	1.1–1.4	2.5–3.1	0.7	2.0–2.3

[a] TBSF, time below the seafloor. Two-way traveltime is converted to depth using layer 2a (2.54 km/s on-axis and 2.63 km/s off-axis) and layer 2b (5.53 km/s) interval velocities derived from the supergather velocity functions (Figure 12). Layer 2a observations for each line are given as mean ± standard deviation, while AMC and Moho observations are given with the range of observations.

4.5. AMC Depth

[35] The depth profile of the magma chamber reflection was found by picking the AMC event on the line 14 stacked and the cross axis stacked and migrated lines and converting the two-way traveltimes into depth using the average layer 2b interval velocity from the three on-axis supergather velocity models (5.55 km/s), in combination with the depth of the layer 2a picks above each AMC pick. The map view locations of these AMC picks are plotted on Figure 3. The depth of the AMC varies between 2.2 and 3.3 km below the seafloor on the along-axis line while the AMC depths on the cross axis lines vary between 2.1 and 3.1 km below the seafloor (details in Table 2).

[36] A 200–600 m range of AMC depths is observed on each cross-axis line due to the dipping nature of the AMC reflector. Using the depth range and the width of each cross-axis AMC event, dips between 8 and 36° are calculated. The dips increase from the northern lines to the southern ones, which reflects the narrower AMC event on (southern) lines 22 and 8 and the greater depth range of the AMC picks from line 8 (Table 2). The 36° dip calculated for line 8 is surprisingly high; however, it reflects picks from one of the weaker migrated AMC events (Figure 10) and therefore may be exaggerated due to the difficulty in picking that event. The 22° dip calculated for line 22 represents a much more robust event (Figure 10); however, its relative narrowness results in a much higher dip for AMC depth ranges similar to those observed on the northern lines.

4.6. Polarity of AMC Event

[37] The polarity of a near-vertical reflection is a diagnostic difference between a cracking front and a magma chamber interface. For a cracking front associated with the downward propagation of a hydrothermally active, thermally fractured regime into a hot but solidified region, an increase in seismic velocities is expected and a reflection from such an interface would be expected to have the same polarity as the first arrival reflection from the seafloor. For an interface of solid rock over a pure melt or partially molten magma chamber, the resultant decrease in seismic velocities results in a polarity reversal for near-vertical reflections.

[38] In order to test the polarity of the Endeavour AMC event, we took traces from the Salty Dawg supergather (Figure 11b) with source-receiver offsets of 0–1.5 km, applied an appropriate normal moveout correction, and summed the traces without applying any filtering at any stage. The result is shown in Figure 11a, where the seafloor reflection and the AMC reflection are highlighted and have opposite polarity, indicating that the AMC reflection is from a negative impedance contrast. The inversion of polarity between these two reflections reinforces our conclusion that the reflector we have identified as an axial magma chamber is not, as previously proposed, a cracking front boundary.

[39] We attempted an amplitude-offset analysis in the intercept time minus slowness ($\tau - \mathrm{p}$) domain to quantify

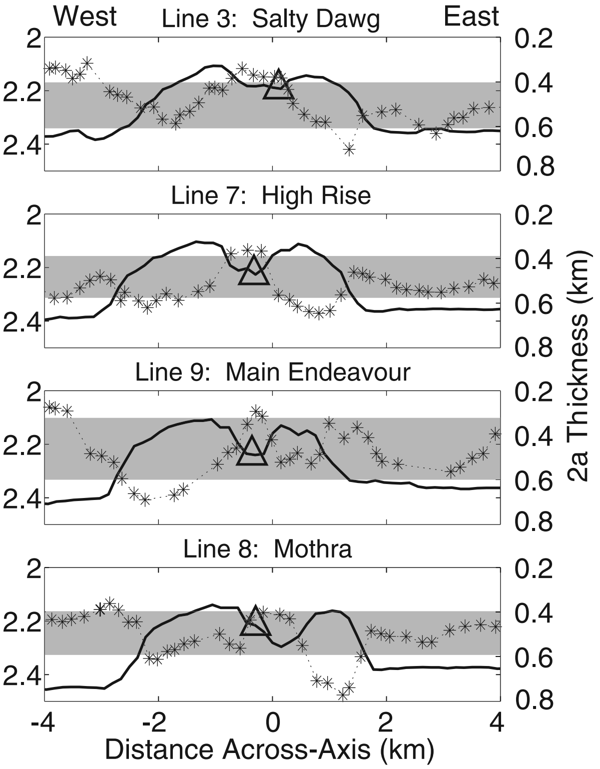

Figure 14. Bathymetry (black line) and layer 2a depths below the seafloor (black stars) from four stacked and migrated cross-axis lines, zoomed in on the central axial high. Black triangles show the location of Endeavour high-temperature vent fields (D. Glickson, personal communication, 2005). Gray boxes show the region of mean ± standard deviation layer 2a thickness for each line.

the crystal versus melt content of the Endeavour AMC at the location of our three along-axis supergathers [e.g., *Collier and Singh*, 1997]. Unfortunately, the AMC reflection at offsets greater than 2 km is highly disrupted by side echoes from the axial graben walls (Figure 11b), making it difficult to differentiate between the amplitude-offset behavior expected for pure molten and partially crystalline magma chamber models.

5. Discussion

5.1. Reconciling the Endeavour AMC With Previous Seismic Studies

[40] Previous seismic studies of the Endeavour Segment failed to definitively locate an axial magma chamber; however, the multichannel reflection profile collected by *Rohr et al.* [1988] does show the same midcrustal axial reflection at the same two-way traveltime that we image. It was not interpreted as an AMC reflection due to the uncertainty in the polarity of the AMC and the lack of a velocity anomaly in the available seismic refraction data.

[41] Previous seismic refraction data [*Cudrak et al.*, 1987; *Cudrak*, 1988; *White and Clowes*, 1990; *Cudrak and Clowes*, 1993] were only sensitive to zones of partial melt (1.5–2.0 km/s velocity reduction relative to surrounding 6.0–6.5 km/s P wave velocity) with cross-axis dimensions greater than 1 km wide and 1 km thick. This resolution would not be sensitive to a thin melt lens such as the AMC reported here (assuming the thickness of the Endeavour AMC is similar to that of the EPR melt lens [*Collier and Singh*, 1998; *Kent et al.*, 1993a]). However, the transition from layer 2c to layer 3 (commonly identified as the transition from sheeted dikes to gabbros formed by crystallization of the magma chamber) occurs at 2.01 km below the seafloor in the *Cudrak and Clowes* [1993] average one-dimensional model, which is roughly coincident with the AMC depths we find in this study.

[42] This leaves the question of why previous refraction studies did not detect a low-velocity region, indicative of high temperatures and partial melt, in the lower crust as described for other magmatic spreading centers [e.g., *Canales et al.*, 2000; *Dunn et al.*, 2001]. The resolution tests for the Endeavour tomography of *White and Clowes* [1990] show significant smearing and poor resolution for features more than 1 km below the seafloor [see *White and Clowes*, 1990, Figure 14]. The forward modeling of *Cudrak and Clowes* [1993] did show a decrease by 0.1–0.2 km/s in seismic layer 3 velocities for seismic waves passing under the axial ridge and attributed this to elevated temperatures but not the presence of partial melt. A new tomographic study of the Endeavour ridge would be useful in distinguishing whether the apparent absence of an EPR-like low-velocity zone under the Endeavour AMC in these prior studies is real or an artifact of data limitations.

5.2. Seismicity and the Axial Magma Chamber

[43] Hypocenters of well-located microseismicity from a 55-day deployment of 15 ocean bottom seismometers (OBSs) on the central Endeavour Ridge [*Wilcock et al.*, 2002] are projected onto our stacked and migrated sections if they are within 0.5 km of our lines (Figures 6 and 10). The positions of the OBSs used to locate the seismicity are shown in Figure 3. We use the events which have been relatively relocated, meaning that closely spaced earthquakes with similar waveforms were cross-correlated to generate self-consistent traveltime picks whose relative errors are much smaller than the absolute errors of individual picks. This results in small relative location errors between events within a swarm (on the order of 100 m) while absolute hypocenter location errors remain on the order of 0.5 km.

[44] Most axial earthquakes are concentrated in a depth range of 1.5–2.7 km. These depths are translated to a two-way traveltime range of 0.7–1.1 s below the seafloor with the velocity function that was used in locating the hypocenters. The seismicity is mostly clustered above the AMC reflector. The appearance of seismicity occurring within the (presumably nonbrittle) regime of the magma chamber is an artifact of location uncertainties and the projection of 3-D event locations onto 2-D lines, which ignores the topography of the dipping magma chamber observed in all cross-axis lines (Figure 10). A 3-D graphic of the seismic lines and the seismicity is available at the Ridge 2000 Data Portal (http://www.marine-geo.org/link/entry.php?id=JdF:Endeavour_VanArk).

[45] In general, the seismicity is distributed diffusely within the observed depth range; however, the cross-axis line which underlies the Salty Dawg vent field also shows seismicity localized along a steeply dipping fault-like plane. The diffuse axial seismicity localized above the AMC reflector may indicate cracking activity in a conductive lid above the melt lens. This would be consistent with the observation that focal mechanisms for axial earthquakes had subhorizontal tension axes oriented in all directions except parallel to the ridge, interpreted as indicating a stress field influenced equally by ridge spreading and hydrothermal cooling [*Wilcock et al.*, 2002].

[46] The axial seismicity seems to be confined to the region above the shallowest portion of the magma chamber (Figures 6 and 10), with much activity beneath the Salty Dawg and High Rise vent fields, a little below the Main Endeavour vent field, and no events beneath the northernmost (Sasquatch) and southernmost (Mothra) vent fields. This may, however, be a sampling bias induced by the seismometer array geometry, variable instrument coupling to the seafloor within the array, and short 2-month time span of the OBS study. Preliminary results of the new Keck Observatory on the Endeavour Ridge [*Wilcock et al.*, 2004] show a similar cluster of hypocenters, but the cluster seems to have moved south slightly with more activity under the Main Endeavour and Mothra vent fields and less under the Salty Dawg vent field.

[47] For two similar experiments in 1995, Endeavour segment microearthquakes were both more numerous and deeper than those observed at the East Pacific Rise, yet the earthquake activity at the two ridges seemed to have similar source mechanisms. In a 3-month OBS deployment at 9°50′N on the EPR, *Sohn et al.* [1998, 1999] detected 283 local microearthquakes which were found to have seismic moments of 10^7–10^9 N m (moment magnitude $M \approx -1$–0). At the Endeavour segment, 1750 microearthquakes with moments of 10^9–4×10^{13} N m (moment magnitude $M \approx 0$–3) were located by *Wilcock et al.* [2002] with data from a shorter, 55-day OBS deployment. The EPR

Table 3. Endeavour Vent Field Temperature and Chemistry Compared to Average Seawater Values and the Depth of the Axial Magma Chamber Under Each Vent Field[a]

	Seawater	Mothra	Main Endeavour	High Rise	Salty Dawg
T	2	304	330–400	315–343	297–329
Cl	540	680	40–505	420–587	710
CO_2	2.3	6	11–26	15–19	18
CH_4	0	1.5	1.5–3.4	2.8–3.4	3.3–3.6
AMC		2.5–3.1	2.1–2.5	2.1–2.3	2.2–2.4

[a] Temperature in °C and chemistry (chlorinity, carbon dioxide concentration, and methane concentration in mmol/kg) are organized from south to north and compared to average seawater values [*Delaney et al.*, 1997; *Kelley et al.*, 2002] and the depth of the axial magma chamber (AMC) under each vent field in kilometers.

hypocenters were located above the 1.5 km deep AMC reflection imaged at that location, clustered between 0.7 and 1.1 km depth. The focal mechanisms and the correlation of earthquake swarms with changes in the chemistry of vents above them suggest that the EPR microseismic events arise from thermal stresses at the base of the hydrothermal system in the shallow crust [*Sohn et al.*, 1998, 1999]. The Endeavour Segment microseismicity is also clustered above the observed magma chamber and also has focal mechanisms suggestive of a thermal cracking mechanism. However, because of the greater depth of the Endeavour AMC, the axial earthquakes are correspondingly deeper [*Wilcock et al.*, 2002]. Preliminary results from more recent OBS experiments at the EPR [*Weekly et al.*, 2005] and Endeavour [*Wilcock et al.*, 2004] indicate that seismicity rates vary greatly over time and are likely related to temporal changes in stress and thermal conditions above the magma lens.

5.3. Hydrothermal Activity and the Axial Magma Chamber

[48] Our results show that all five large, high-temperature Endeavour hydrothermal vent fields are underlain by an axial magma chamber (Figures 6 and 10). We therefore looked for correlations between the geometry and properties of the AMC and the location and activity of the vents. The focusing of Endeavour seismicity and hydrothermal vents above the shallowest part of the AMC (Figure 6), combined with the cracking focal mechanisms of the microseismic events might reflect a "chimney effect" with upflow of hydrothermal fluid channelled predominantly above the shallowest areas of the magma chamber heat source. However, a hydrographic survey of the Endeavour ridge [*Veirs et al.*, 1999] found possible hydrothermal sources south of Mothra as far as 47°54′N. More exploratory studies looking for high-temperature hydrothermal outflow and their vent sources above the deeper, southern portion of the AMC (CMPs 6600–6950 on Figure 6, latitudes 47°52.2′–47°53.8′N) would help to determine whether the apparent focusing of hydrothermal flow above the shallowest portion of the AMC is real or merely a sampling artifact.

[49] There is no simple relationship between Endeavour magma chamber depth and vent temperatures and chlorinities (Table 3) [*Butterfield et al.*, 1994; *Delaney et al.*, 1997; *Kelley et al.*, 2002]. The AMC is approximately the same depth range (~2.1–2.4 km on each cross-axis line) beneath all the Endeavour hydrothermal vent fields except Mothra (2.5–3.1 km), and the range of published temperatures and chlorinity values within each well-sampled vent field is as large as the differences between the fields. There might be a correlation between lower CO_2 values at Mothra and the deeper AMC below that location (Table 3). More observations would be useful to constrain this possible relationship. There is no clear correlation between published methane concentrations at the various vent fields and AMC depth. While many more chemical components of vent fluids have been studied within specific vent fields, especially the Main Endeavour vent field [*Lilley et al.*, 2003], cross-field observations on the large spatial scale necessary for comparison with Endeavour AMC depths have not been published.

[50] In general, our preliminary comparison suggests that AMC depth is not a dominant factor in determining vent fluid properties. In particular, temperature and chlorinity are probably controlled instead by phase separation, subsurface mixing of hydrothermal fluids and seawater, and other complexities of the circulation path through the crust [*Butterfield et al.*, 1994; *Delaney et al.*, 1997; *Bach and Humphris*, 1999; *Kelley et al.*, 2002]. A recent study has tied the 1999 earthquake swarms to magmatic volatile signatures in Main Endeavour vent fluids [*Lilley et al.*, 2003], which indicates that magmatic diking and eruption activity may influence vent fluid properties even if the depth of the magma chamber does not [see also *Butterfield and Mossoth*, 1994; *Butterfield et al.*, 1997; *Von Damm*, 2000].

5.4. Ridge System Comparisons

[51] Table 4 presents a comparison of on- and off-axis layer 2a thickness and axial magma chamber depth and width for the fast spreading East Pacific Rise (EPR) [*Kent et al.*, 1993b, 1994; *Hooft et al.*, 1997; *Carbotte et al.*, 2000] and four intermediate spreading systems: the Juan de Fuca Ridge (our Endeavour segment results and *Canales et al.* [2005]), the Southeast Indian Ridge (SEIR) [*Baran et al.*, 2005], the Galapagos Spreading Center (GSC) [*Detrick et al.*, 2002b; *Blacic et al.*, 2004], and the Lau back-arc spreading centers [*Jacobs et al.*, 2003].

[52] The Endeavour axial layer 2a thickness is greater in magnitude and variability than that of the EPR and the Vance and Cleft segments of the Juan de Fuca Ridge; however, it is similar to that of the GSC, the portions of the SEIR with a rifted axial high, and the Central Lau Spreading Center (CLSC). The Endeavour axial layer 2a is thinner than that found on the portions of the SEIR with a shallow axial valley and the Eastern Lau Spreading Center and Valu Fa Ridge (ELSC/VFR). While off-axis 2a thickening is observed for most of the ridge systems presented in Table 4, the Endeavour layer 2a cross-axis variability shows

Table 4. Comparison of On- and Off-Axis Layer 2a Thickness, AMC Depth, and AMC Width for Various Spreading Ridges[a]

	Layer 2a Thickness		Axial Magma Chamber	
	On-Axis, km	Off-Axis, km	Depth, km	Width, km
Galapagos Spreading Center, 4.5–5.6 cm/yr				
E. GSC[b]	0.24–0.42	0.4–0.7	∼1.0–2.5	0.5–1.5
W. GSC[c]	0.36–0.60	0.35–0.65	2.5–4.5	0.7–2.4
Juan de Fuca Ridge, 5.6–5.7 cm/yr				
Endeavour	0.38 ± 0.12	0.50 ± 0.11	2.1–3.3	0.4–1.2
Vance	0.30–0.35	0.5–0.6	2.4–2.7	0.6–1.7
Cleft	0.25–0.30	0.5–0.6	2.0–2.3	0.6–1.7
Southeast Indian Ridge,[d] 7.2–7.6 cm/yr				
Axial high	∼0.31	thicker	∼1.5	—
Rifted axial high	∼0.46	same	∼2.1	—
Shallow axial valley	∼0.45, ∼0.80	same	No AMC	—
Lau Back-Arc Basin, 4.0–9.0 cm/yr				
CLSC (faster)[e]	0.38	—	1.49	—
N. ELSC[e]	0.51	—	No AMC	—
C. ELSC[e]	0.62–0.74	—	2.18–2.34	—
VFR (slower)[e]	0.66–1.00	—	2.35–2.82	—
East Pacific Rise				
15°30′–17°N (8.5 cm/yr)	0.16–0.31	0.34–0.53	1.4–1.7	0.25–1.7
9°17′–9°53N	0.18–0.38	0.44–0.56	1.42–1.56	0.25–4.15
14°–14°30 s (>15 cm/yr)	0.19–0.28	0.51–0.57	0.94–1.25	0.375–1.05
17°4′–20°10 s	0.20–0.33	0.35–0.62	0.76–1.55	0.375–1.54

[a] Ridges include the Endeavour (this study), Cleft, and Vance segments of the Juan de Fuca Ridge [*Canales et al.*, 2005], the Galapagos Spreading Center (GSC) [*Blacic et al.*, 2004], the Southeast Indian Ridge (SEIR) [*Baran et al.*, 2005], the Lau back-arc spreading system [*Jacobs et al.*, 2003], and the East Pacific Rise (EPR) [*Kent et al.*, 1993b, 1994; *Hooft et al.*, 1997; *Carbotte et al.*, 2000]. The full spreading rate for each ridge system is also given [*Wilson*, 1993; *DeMets et al.*, 1994; *Blacic et al.*, 2004; *Baran et al.*, 2005]. Dashes indicate that the appropriate measurement was not available for that system.

[b] Hot spot influenced portion of the GSC, east of 92.5°W.

[c] Non–hot spot influenced portion of the GSC, west of 92.5°W.

[d] Results for SEIR are categorized by surface morphology of the ridge [*Baran et al.*, 2005].

[e] CLSC, Central Lau Spreading Center; axial high morphology. N. ELSC, Northern Eastern Lau Spreading Center; rifted axis. C. ELSC, Central Eastern Lau Spreading Center; rounded axial high. VFR, Value Fa Ridge; blade-like morphology due to high- viscosity lavas resulting from a subduction component in the magma.

no such clear pattern, the western portion of the GSC has limited off-axis 2a thickening, and the rifted axial high and shallow axial valley portions of the SEIR [*Baran et al.*, 2005] are not observed to have significant off-axis layer 2a thickness increases.

[53] Why does layer 2a thicken off-axis on some ridge systems and not on others? Several authors have suggested that the difference is due to the interplay between magma supply and ridge topography [*Mutter et al.*, 1995; *Carbotte et al.*, 1998; *Blacic et al.*, 2004; *Canales et al.*, 2005]. The ridge topography is controlled by a combination of tectonic extension, flexure, and volcanic construction. In turn, the slope of the axial high and the depth of the axial summit graben promote or hinder the flow of volcanic eruptions off-axis which leads to layer 2a thickening. Large variability in off-axis 2a thickness is found on the parts of the GSC which have a narrow (<0.8 km) AMC [*Blacic et al.*, 2004], perhaps reflecting lower magma supply. This is similar to the variability observed on all the cross-axis Endeavour lines, independent of AMC width.

[54] The range of AMC widths observed at many different places on the mid-ocean ridge system (Table 4) seems to be a relatively constant ∼0.5–1.5 km, with values as low as 0.25 and as high as 4.15 on the EPR [*Kent et al.*, 1993b, 1994; *Hooft et al.*, 1997; *Carbotte et al.*, 2000]. Our Endeavour AMC width observations of 0.5–1.2 km fall within this range. The lack of correlation between spreading rate and AMC width stands in contrast to AMC depth observations, which do seem to inversely correlate with spreading rate [*Purdy et al.*, 1992]. The southern portion of the EPR (full spreading rate >15 cm/yr) has the shallowest AMC depths [*Hooft et al.*, 1997] while the non–hot spot influenced western portion of the GSC (full spreading rate 4.5–5.6 cm/yr) has the deepest AMC observed to date [*Blacic et al.*, 2004]. The Endeavour AMC is significantly deeper than the fast spreading AMC depths, but comparable to depths found along other intermediate spreading ridges with similar ridge morphologies.

[55] A combination of spreading rate and ridge morphology seems to be a better predictor of subsurface similarities between ridges than spreading rate values alone. The Juan de Fuca Ridge has similar spreading rates to the Galapagos Spreading Center and the Southeast Indian Ridge; however, those ridge systems are both heavily influenced by nearby mantle temperature anomalies. The eastern portion of the GSC is strongly influenced by the Galapagos hot spot [*Detrick et al.*, 2002b; *Blacic et al.*, 2004], while the SEIR has strong changes in ridge morphology and subsurface crustal structure correlated with distance from the Australian Antarctic Discordance area of cold mantle [*Baran et al.*, 2005]. The Endeavour segment crustal structure is similar to portions of those ridges, but only where the ridge morphology indicates a similar thermal state in the crust and upper mantle.

5.5. Intermediate Spreading Ridge Heat Extraction

[56] The existence of a magma chamber beneath the Endeavour Ridge indicates that heat is supplied at this

intermediate spreading ridge by the same magmatic source as at fast spreading ridges such as the East Pacific Rise. There is no need to invoke a cracking front propagating down into and mining heat from an area of hot but unmolten rock in the lower crust [*Wilcock and Delaney*, 1996]. The observed differences between small, short-lived, magmatically controlled hydrothermal systems on the EPR and larger, longer-lived, fault-controlled hydrothermal systems on the Endeavour Segment still require explanation, however. We propose a hybrid model of heat extraction for intermediate spreading ridges which combines the magmatic heat source of the fast spreading ridge and the fault-controlled hydrothermal circulation of the slow spreading ridge model (Figure 1). However, the source of the faulting remains a subject of debate.

[57] In general, the observed Endeavour magma chamber depths are consistent with model predictions from numerical studies relating half spreading rate to depth to the top of a steady state magma lens through the thermal balance between heat supply from magmatic crustal injection and cooling due to hydrothermal circulation [*Phipps Morgan and Chen*, 1993; *Chen and Lin*, 2004]. These models depend on the supposition that magma rises within the oceanic crust due to buoyancy forces or viscous pressures until it reaches a freezing horizon where it ponds into a quasi steady state magma lens. The axial morphology and faulting above the magma lens are a function of the thermal structure, which determines the thickness of the axial lithosphere and therefore the yield strength of the axial lithosphere as it is pulled apart. According to this model, the Endeavour axial summit graben and the faults which bound it and provide permeability pathways for the hydrothermal circulation are the result of tectonic extensional stresses interacting with a cooler upper crust due to a deeper magma chamber.

[58] Another model for the evolving axial topography on the Juan de Fuca Ridge emphasizes the contribution of dike intrusion to subsidence and fault slip at the seafloor due to feedback between the rheology of the crust above a magma sill and dike intrusion [*Carbotte et al.*, 2006]. Within the framework of this model, the faulting related permeability pathways which sustain Endeavour's massive, high-temperature hydrothermal vent fields are a result of the interaction between the regional tectonic extension and stress perturbations due to dike intrusions from the axial magma chamber. The tensional regime of this model could lead to the higher microseismicity levels on Endeavour discussed in section 5.2. That small-scale fracturing is needed to keep the upgoing hydrothermal pathways open in the face of ongoing quartz precipitation in the upwelling portion of the hydrothermal system [*Wilcock and Delaney*, 1996].

[59] A final paradox is presented by the *Wilcock and Delaney* [1996] estimate that the heat flux from the Main Endeavour vent field is between 5 and 50 times the steady state heat flux necessary to solidify and cool a 6-km-thick crust. They calculate that mining this amount of heat from a 2-km-wide AMC would require a conductive boundary only ~1-m-thick, which they interpret to be implausibly thin. One possible resolution is that the heat flux has been overestimated, or that the portion of the ridge which is cooled by the subsurface circulation cell supplying each vent field has been underestimated. Another possible solution is that the cracking front model proposed by *Wilcock and Delaney* [1996] is locally correct on the margins of the imaged magma chambers, perhaps resulting in the apparent segmentation of the Endeavour AMC (although that could also be an artifact of streamer feathering, topographic effects on the data or attempting to image a narrow three-dimensional body with a one-dimensional line). Possible issues with the flux estimate may be resolved by further heat flux measurements and modeling, while the possible segmentation of the Endeavour AMC would be fully revealed with a three-dimensional multichannel seismic reflection survey.

6. Conclusions

[60] Multichannel seismic reflection data gathered on the Endeavor segment of the Juan de Fuca Ridge during July 2002 reveal the presence of a crustal magma body underlying all five known hydrothermal vent fields of the Endeavour segment. The magma body is relatively deep (2.1–3.3 km) and narrow (0.4–1.2 km wide), and appears to be segmented into multiple crustal magma lenses adding up to a total along-axis distance of 16–24 km.

[61] The polarity of the reflection from the top of the AMC combined with similarities to well-studied AMC events at other ridges confirms that the reflection is due to a decrease in seismic velocities at the top of a magma chamber rather than a hydrothermal cracking front. Microseismicity within 0.5 km of the axis is mostly confined to a region above the shallowest portions of the AMC. We interpret the thermal cracking focal mechanisms of the microseismic events as hydrothermal circulation penetrating into a conductive lid above a magma lens which is continually replenished with new magma from below. Cross axis lines show the magma chamber to be dipping from the west to the east, with the vent fields located over shallower portions of the AMC.

[62] The AMC is approximately the same depth (dipping from ~2.1 to 2.4 km) beneath all the Endeavour hydrothermal vent fields except Mothra (2.5–3.1 km), and the range of temperatures and chemistry values within each well-sampled vent field tends to be larger than the differences between the fields. Our results suggest that AMC depth is not a dominant factor in determining vent fluid properties, which are probably controlled instead by phase separation, subsurface mixing of hydrothermal fluids and seawater, and other complexities of the circulation path through the crust.

[63] Hydrothermal systems at the intermediate spreading Endeavour Segment, like those at fast spreading ridges, appear to be driven by heat extraction from a crustal magma body. Morphological, hydrothermal, and seismic differences between the intermediate spreading Endeavour and the fast spreading EPR are attributable either to the greater depth of the Endeavour AMC and the correspondingly cooler, more brittle shallow crust overlying the magma chamber or to faulting controlled by dike intrusions from the axial magma chamber.

[64] **Acknowledgments.** E.V.A. was supported by a National Science Foundation Graduate Research Fellowship, the WHOI-MIT Joint Program, and the WHOI Deep Ocean Exploration Institute. This work was also supported by OCE-0002551 to the Woods Hole Oceanographic Institution,

OCE-0002488 to Lamont-Doherty Earth Observatory, and OCE-0002600 to Scripps Institution of Oceanography. The authors would like to acknowledge the many contributions of the science party and crew of the R/V *Maurice Ewing*'s EW0207 leg. This paper benefited greatly from suggestions by Gail Christeson and an anonymous reviewer. In addition, the authors would like to thank John Collins, Satish Singh, Rob Sohn, and the participants of the Ridge 2000 program's 2005 Cyprus field school for helpful conversations.

References

Alt, J. C. (1995), Subseafloor processes in mid-ocean ridge hydrothermal systems, in *Seafloor Hydrothermal Systems: Physical, Chemical, Biological, and Geological Interactions*, *Geophys. Monogr. Ser.*, vol. 91, edited by S. E. Humphris et al., pp. 85–114, AGU, Washington, D. C.

Bach, W., and S. E. Humphris (1999), Relationship between the Sr and O isotope compositions of hydrothermal fluids and the spreading and magma-supply rates at oceanic spreading centers, *Geology*, *27*, 1067–1070.

Baker, E. T., et al. (2002), Hydrothermal venting along Earth's fastest spreading center: East Pacific Rise, 27.5°–32.3°S, *J. Geophys. Res.*, *107*(7), 2130, doi:10.1029/2001JB000651.

Baran, J. M., J. R. Cochran, S. M. Carbotte, and M. Nedimovic (2005), Variations in upper crustal structure due to variable mantle temperature along the Southeast Indian Ridge, *Geochem. Geophys. Geosyst.*, *6*, Q11002, doi:10.1029/2005GC000943.

Barclay, A. H., and W. S. D. Wilcock (2004), Upper crustal seismic velocity structure and microearthquake depths at the Endeavour Segment, Juan de Fuca Ridge, *Geochem. Geophys. Geosyst.*, *5*, Q01004, doi:10.1029/2003GC000604.

Bhat, V., P. R. Shaw, and J. R. Delaney (1997), The Endeavour Ridge as observed by DSL120 sidescan sonar: Interplay of volcanic, tectonic, and hydrothermal processes, *Eos Trans. AGU*, *78*(46), Fall Meet. Suppl., F805.

Blacic, T. M., G. T. Ito, J. P. Canales, R. S. Detrick, and J. M. Sinton (2004), Constructing the crust along the Galapagos Spreading Center 91.3°–95.5°W: Correlation of seismic layer 2a with axial magma lens and topographic characteristics, *J. Geophys. Res.*, *109*, B10310, doi:10.1029/2004JB003066.

Bohnenstiehl, D. R., R. P. Dziak, M. Tolstoy, C. G. Fox, and M. Fowler (2004), Temporal and spatial history of the 1999–2000 Endeavour Segment seismic series, Juan de Fuca Ridge, *Geochem. Geophys. Geosyst.*, *5*, Q09003, doi:10.1029/2004GC000735.

Buck, W. R., S. M. Carbotte, and C. Z. Mutter (1997), Controls on extrusion at mid-ocean ridges, *Geology*, *25*, 935–938, doi:10.1130/0091-7613(1997)025<0935:COEAMO>2.3.CO;2.

Butterfield, D. A., and G. J. Mossoth (1994), Geochemistry of north Cleft segment vent fluids: Temporal changes in chlorinity and their possible relation to recent volcanism, *J. Geophys. Res.*, *99*, 4951–4968.

Butterfield, D. A., R. E. McDuff, M. J. Mottl, M. D. Lilley, J. E. Lupton, and G. J. Massoth (1994), Gradients in the composition of hydrothermal fluids from the Endeavour Segment vent field: Phase separation and brine loss, *J. Geophys. Res.*, *99*, 9561–9583.

Butterfield, D. A., et al. (1997), Seafloor eruptions and evolution of hydrothermal fluid chemistry, *Philos. Trans. R. Soc. London, Ser. A*, *355*, 369–386.

Canales, J. P., J. A. Collins, J. Escartn, and R. S. Detrick (2000), Seismic structure across the rift valley of the Mid-Atlantic Ridge at 23°20′ (MARK area): Implications for crustal accretion processes at slow spreading ridges, *J. Geophys. Res.*, *105*, 28,411–28,426.

Canales, J. P., R. S. Detrick, S. M. Carbotte, G. M. Kent, J. B. Diebold, A. Harding, J. Babcock, M. Nedimovic, and E. V. Ark (2005), Upper crustal structure and axial topography at intermediate spreading ridges: Seismic constraints from the southern Juan de Fuca Ridge, *J. Geophys. Res.*, *110*, B12104, doi:10.1029/2005JB003630.

Cann, J. R., and M. R. Strens (1989), Modeling periodic megaplume emission by black smoker systems, *J. Geophys. Res.*, *94*, 12,227–12,237.

Carbotte, S., C. Mutter, J. Mutter, and G. Ponce-Correa (1998), Influence of magma supply and spreading rate on crustal magma bodies and emplacement of the extrusive layer: Insights from the East Pacific Rise at lat 16°N, *Geology*, *26*, 455–458, doi:10.1130/0091-7613(1998)026<0455:IOMSAS>2.3.CO;2.

Carbotte, S. M., A. Solomon, and G. Ponce-Correa (2000), Evaluation of morphological indicators of magma supply and segmentation from a seismic reflection study of the East Pacific Rise 15°30′–17°N, *J. Geophys. Res.*, *105*, 2737–2759.

Carbotte, S., et al. (2002), A multi-channel seismic investigation of ridge crest and ridge flank structure along the Juan de Fuca Ridge, *Eos Trans. AGU*, *83*(47), Fall Meet. Suppl., Abstract T72C–07.

Carbotte, S. M., R. S. Detrick, A. Harding, J. P. Canales, J. Babcock, G. Kent, E. V. Ark, M. Nedimovic, and J. Diebold (2006), Rift topography linked to magmatism at the intermediate spreading Juan de Fuca Ridge, *Geology*, *34*, 209–212, doi:10.1130/G21969.1.

Chen, Y. J., and J. Lin (2004), High sensitivity of ocean ridge thermal structure to changes in magma supply: The Galápagos Spreading Center, *Earth Planet. Sci. Lett.*, *221*, 263–273, doi:10.1016/S0012-821X(04)00099-8.

Collier, J. S., and M. C. Sinha (1992), Seismic mapping of a magma chamber beneath the Valu Fa Ridge, Lau Basin, *J. Geophys. Res.*, *97*, 14,031–14,053.

Collier, J. S., and S. C. Singh (1997), Detailed structure of the top of the melt body beneath the East Pacific Rise at 9°40′N from waveform inversion of seismic reflection data, *J. Geophys. Res.*, *102*, 20,287–20,304.

Collier, J. S. and S. C. Singh (1998), A seismic inversion study of the axial magma chamber reflector beneath the East Pacific Rise near 10°N, in *Modern Ocean Floor Processes and the Geological Record*, edited by R. A. Mills, *Geol. Soc. Spec. Publ.*, *148*, 17–28.

Cudrak, C. F. (1988), Shallow crustal structure of the Endeavour Ridge Segment, Juan de Fuca Ridge, from a detailed seismic refraction survey, M.S. thesis, Univ. of B. C., Vancouver, B. C., Canada.

Cudrak, C. F., and R. M. Clowes (1993), Crustal structure of Endeavour Ridge Segment, Juan de Fuca Ridge, from a detailed seismic refraction survey, *J. Geophys. Res.*, *98*, 6329–6349.

Cudrak, C. F., D. J. White, and R. M. Clowes (1987), A 3-D seismic refraction survey of crustal structure, Endeavour Segment, Juan de Fuca Ridge, *Eos Trans. AGU*, *68*, 1371.

Delaney, J. R., R. E. McDuff, V. Robigou, A. Schultz, M. Smith, J. Wells, V. A. Atnipp, and J. McClain (1990), Covariation in microseismicity and hydrothermal output in the Endeavour vent field, *Eos Trans. AGU*, *71*, 1609.

Delaney, J. R., V. Robigou, R. E. McDuff, and M. K. Tivey (1992), Geology of a vigorous hydrothermal system on the Endeavour Segment, Juan de Fuca Ridge, *J. Geophys. Res.*, *97*, 19,663–19,682.

Delaney, J. R., D. S. Kelley, M. D. Lilley, D. A. Butterfield, R. E. McDuff, J. A. Baross, J. W. Deming, H. P. Johnson, and V. Robigou (1997), The Endeavour hydrothermal system I: Cellular circulation above an active cracking front yields large sulfide structures, "fresh" vent water, and hyperthermophilic archaea, *RIDGE Events*, *8*, 11–19.

DeMets, C., R. G. Gordon, D. F. Argus, and S. Stein (1994), Effect of recent revisions to the geomagnetic reversal timescale on estimates of current plate motions, *Geophys. Res. Lett.*, *21*, 2191–2194.

Detrick, R. S., S. Carbotte, E. M. V. Ark, J. P. Canales, G. Kent, A. Harding, J. Diebold, and M. Nedimovic (2002a), New multichannel seismic constraints on the crustal structure of the Endeavour Segment, Juan de Fuca Ridge: Evidence for a crustal magma chamber, *Eos Trans. AGU*, *83*(47), Fall Meet. Suppl., Abstract T12B–1316.

Detrick, R. S., et al. (2002b), Correlated geophysical, geochemical, and volcanological manifestations of plume-ridge interaction along the Galápagos Spreading Center, *Geochem. Geophys. Geosyst.*, *3*(10), 8501, doi:10.1029/2002GC000350.

Dunn, R. A., D. R. Toomey, R. S. Detrick, and W. S. D. Wilcock (2001), Continuous mantle melt supply beneath an overlapping spreading center on the East Pacific Rise, *Science*, *291*, 1955–1958, doi:10.1126/science.1057683.

Fornari, D. J. and R. W. Embley (1995), Tectonic and volcanic controls on hydrothermal processes at the mid-ocean ridge: An overview based on near-bottom and submersible studies, in *Seafloor Hydrothermal Systems: Physical, Chemical, Biological, and Geological Interactions*, *Geophys. Monogr. Ser.*, vol. 91, edited by S. E. Humphris et al., pp. 1–46, AGU, Washington, D. C.

Hannington, M. D., I. R. Jonasson, P. M. Herzig, and S. Petersen (1995), Physical and chemical processes of seafloor mineralization at mid-ocean ridges, in *Seafloor Hydrothermal Systems: Physical, Chemical, Biological, and Geological Interactions*, *Geophys. Monogr. Ser.*, vol. 91, edited by S. E. Humphris et al., pp. 115–157, AGU, Washington, D. C.

Harding, A. J., G. M. Kent, and J. A. Orcutt (1993), A multichannel seismic investigation of upper crustal structure at 9°N on the East Pacific Rise: Implications for crustal accretion, *J. Geophys. Res.*, *98*, 13,925–13,944.

Haymon, R. M., D. J. Fornari, M. H. Edwards, S. Carbotte, D. Wright, and K. C. Macdonald (1991), Hydrothermal vent distribution along the East Pacific Rise crest (9°09′–54′N) and its relationship to magmatic and tectonic processes on fast-spreading mid-ocean ridges, *Earth Planet. Sci. Lett.*, *104*, 513–534.

Haymon, R. M., et al. (1993), Volcanic eruption of the mid-ocean ridge along the East Pacific Rise crest at 9°45–52′N: Direct submersible observations of seafloor phenomena associated with an eruption event in April, 1991, *Earth Planet. Sci. Lett.*, *119*, 85–101.

Holmes, M. L., and H. P. Johnson (1993), Upper crustal densities derived from sea floor gravity measurements: Northern Juan de Fuca Ridge, *Geophys. Res. Lett.*, *20*, 1871–1874.

Hooft, E. E. E., R. S. Detrick, and G. M. Kent (1997), Seismic structure and indicators of magma budget along the southern East Pacific Rise, *J. Geophys. Res.*, *102*, 27,319–27,340.

Jacobs, A. M., A. J. Harding, G. M. Kent, and J. A. Collins (2003), Along-axis crustal structure of the Lau Back-Arc Basin from multichannel seismic observations, *Eos Trans. AGU*, *84*(46), Fall Meet. Suppl., Abstract B12A–0728.

Johnson, H. P., K. Becker, and R. P. V. Herzen (1993), Near-axis heat flow measurements on the northern Juan de Fuca Ridge: Implications for fluid circulation in oceanic crust, *Geophys. Res. Lett.*, *20*, 1875–1878.

Johnson, H. P., M. Hutnak, R. P. Dziak, C. G. Fox, I. Urcuyo, J. P. Cowen, J. Nabelek, and C. Fisher (2000), Earthquake-induced changes in a hydrothermal system on the Juan de Fuca mid-ocean ridge, *Nature*, *407*, 174–177.

Kadko, D. C., N. D. Rosenberg, J. E. Lupton, R. W. Collier, and M. D. Lilley (1990), Chemical reaction rates and entrainment within the Endeavour Ridge hydrothermal plume, *Earth Planet. Sci. Lett.*, *99*, 315–335.

Kappel, E. S., and W. B. F. Ryan (1986), Volcanic episodicity and a non-steady state rift valley along northeast Pacific spreading centers: Evidence from Sea MARC I, *J. Geophys. Res.*, *91*, 13,925–13,940.

Karsten, J. L., S. R. Hammond, E. E. Davis, and R. G. Currie (1986), Detailed geomorphology and neotectonics of the Endeavour Segment, Juan de Fuca Ridge: New results from Seabeam swath mapping, *Geol. Soc. Am. Bull.*, *97*, 213–221.

Karsten, J. L., J. R. Delaney, J. M. Rhodes, and R. A. Liias (1990), Spatial and temporal evolution of magmatic systems beneath the Endeavour Segment, Juan de Fuca Ridge: Tectonic and petrologic constraints, *J. Geophys. Res.*, *95*, 19,235–19,256.

Kelley, D. S., J. R. Delaney, and D. R. Yoerger (2001), Geology and venting characteristics of the Mothra hydrothermal field, Endeavour Segment, Juan de Fuca Ridge, *Geology*, *29*, 959–962, doi:10.1130/0091-7613(2001)0290959:GAVCOT2.0.CO;2.

Kelley, D. S., J. A. Baross, and J. R. Delaney (2002), Volcanoes, fluids, and life at mid-ocean ridge spreading centers, *Annu. Rev. Earth Planet. Sci.*, *30*, 385–491, doi:10.1146/annurev.earth.30.091201.141331.

Kelley, D. S., J. R. Delaney, M. D. Lilley, D. A. Butterfield, and J. D. Baross (2003), Geological, biological, and chemical linkages within the Endeavour hydrothermal system, in *Geoscience Horizons: Seattle 2003: Abstracts With Programs*, vol. 35, p. 220, Geol. Soc. of Am., Boulder, Colo.

Kent, G. M., A. J. Harding, and J. A. Orcutt (1993a), Distribution of magma beneath the East Pacific Rise near the 9 degrees 03′N overlapping spreading center from forward modeling of common depth point data, *J. Geophys. Res.*, *98*, 13,971–13,995.

Kent, G. M., A. J. Harding, and J. A. Orcutt (1993b), Distribution of magma beneath the East Pacific Rise between the Clipperton Transform and the 9 degrees 17′N Deval from forward modeling of common depth point data, *J. Geophys. Res.*, *98*, 13,945–13,969.

Kent, G. M., A. J. Harding, J. A. Orcutt, R. S. Detrick, J. C. Mutter, and P. Buhl (1994), Uniform accretion of oceanic crust south of the Garrett Transform at 14 degrees 15′S on the East Pacific Rise, *J. Geophys. Res.*, *99*, 9097–9116.

Kent, G. M., I. I. Kim, A. J. Harding, R. S. Detrick, and J. A. Orcutt (1996), Suppression of sea-floor-scattered energy using a dip-moveout approach: Application to the mid-ocean ridge environment, *Geophysics*, *61*, 821–834.

Lilley, M. D., M. C. Landsteiner, E. A. McLaughlin, C. B. Parker, A. S. M. Cherkaoui, G. Lebon, S. R. Viers, and J. R. Delaney (1995), Real-time mapping of hydrothermal plumes on the Endeavor Segment of the Juan de Fuca, *Eos Trans. AGU*, *76*(46), Fall Meet. Suppl., F420.

Lilley, M. D., D. A. Butterfield, J. E. Lupton, and E. J. Olson (2003), Magmatic events can produce rapid changes in hydrothermal vent chemistry, *Nature*, *422*, 878–881, doi:10.1038/nature01569.

Lister, C. R. B. (1974), On the penetration of water into hot rock, *Geophys. J. R. Astron. Soc.*, *39*, 465–509.

Lister, C. R. B. (1980a), Heat flow and hydrothermal circulation, *Annu. Rev. Earth Planet. Sci.*, *8*, 95–117.

Lister, C. R. B. (1980b), Rock and water histories during sub-oceanic hydrothermal events, *Oceanol. Acta*, *4*, suppl., 41–46.

Lister, C. R. B. (1982), "Active" and "passive" hydrothermal systems in the oceanic crust: Predicted physical conditions, in *The Dynamic Environment of the Ocean Floor*, edited by K. A. Fanning and F. T. Manheim, pp. 441–470, D. C. Heath, Lexington, Mass.

Lowenthal, D., L. Lu, R. Roberson, and J. Sherwood (1976), The wave equation applied to migration, *Geophys. Prospect.*, *24*, 380–399.

McClain, J. S., M. L. Begnaud, M. A. Wright, J. Fondrk, and G. K. V. Damm (1993), Seismicity and tremor in a submarine hydrothermal field: The northern Juan de Fuca Ridge, *Geophys. Res. Lett.*, *20*, 1883–1886.

Mutter, J. C., S. M. Carbotte, W. Su, L. Xu, P. Buhl, R. S. Detrick, G. M. Kent, J. A. Orcutt, and A. J. Harding (1995), Seismic images of active magma systems beneath the East Pacific Rise between 17°05′ and 17°35′S, *Science*, *268*, 391–395.

Nedimovic, M. R., S. Mazzotti, and R. D. Hyndman (2003), Three-dimensional structure from feathered two-dimensional marine seismic reflection data: The eastern Nankai Trough, *J. Geophys. Res.*, *108*(B10), 2456, doi:10.1029/2002JB001959.

Nedimovic, M. R., S. M. Carbotte, A. J. Harding, R. S. Detrick, J. P. Canales, J. B. Diebold, G. M. Kent, M. Tischer, and J. M. Babcock (2005), Frozen magma lenses below the oceanic crust, *Nature*, *436*, 1149–1152, doi:10.1038/nature03944.

Phipps Morgan, J., and Y. J. Chen (1993), The genesis of oceanic crust: Magma injection, hydrothermal circulation, and crustal flow, *J. Geophys. Res.*, *98*, 6283–6297.

Purdy, G. M., L. S. L. Kong, G. L. Christeson, and S. C. Solomon (1992), Relationship between spreading rate and the seismic structure of mid-ocean ridges, *Nature*, *355*, 815–817, doi:10.1038/355815a0.

Robigou, V., J. R. Delaney, and D. S. Stakes (1993), Large massive sulphide deposits in a newly discovered active hydrothermal system, the High-Rise Field, Endeavour Segment, Juan de Fuca Ridge, *Geophys. Res. Lett.*, *20*, 1887–1890.

Rohr, K. M. M., B. Milkereit, and C. J. Yorath (1988), Asymmetric deep crustal structure across the Juan de Fuca Ridge, *Geology*, *16*, 533–537.

Sarrazin, J., V. Robigou, S. K. Juniper, and J. R. Delaney (1997), Biological and geological dynamics over four years on a high-temperature sulfide structure at the Juan de Fuca Ridge hydrothermal observatory, *Mar. Ecol. Prog. Ser.*, *153*, 5–24.

Sohn, R. A., D. J. Fornari, K. L. V. Damm, J. A. Hildebrand, and S. C. Webb (1998), Seismic and hydrothermal evidence for a cracking event on the East Pacific Rise crest at 9°50′N, *Nature*, *396*, 159–161.

Sohn, R. A., J. A. Hildebrand, and S. C. Webb (1999), A microearthquake survey of the high-temperature vent fields on the volcanically active East Pacific Rise, *J. Geophys. Res.*, *104*, 25,367–25,377.

Sours-Page, R., K. T. M. Johnson, R. L. Nielsen, and J. L. Karsten (1999), Local and regional variation of MORB parent magmas: Evidence from melt inclusions from the Endeavour Segment of the Juan de Fuca Ridge, *Contrib. Mineral. Petrol.*, *134*, 342–363.

Thomson, R. E., J. R. Delaney, R. E. McDuff, D. R. Janecky, and J. S. McClain (1992), Physical characteristics of the Endeavour Ridge hydrothermal plume during July 1988, *Earth Planet. Sci. Lett.*, *111*, 141–154.

Tivey, M. A., and H. P. Johnson (1987), The Central Anomaly Magnetic High: Implications for ocean crust construction and evolution, *J. Geophys. Res.*, *92*, 12,685–12,694.

Tivey, M. A., and H. P. Johnson (2002), Crustal magnetization reveals subsurface structure of Juan de Fuca Ridge hydrothermal vent fields, *Geology*, *30*, 979–982, doi:10.1130/0091-7613(2002)030<0979:CMRSSO>2.0.CO;2.

Tivey, M. K., and J. R. Delaney (1986), Growth of large sulfide structures on the Endeavour Segment of the Juan de Fuca Ridge, *Earth Planet. Sci. Lett.*, *77*, 303–317.

Tivey, M. K., D. S. Stakes, T. L. Cook, M. D. Hannington, and S. Petersen (1999), A model for growth of steep-sided vent structures on the Endeavour Segment on the Juan de Fuca Ridge: Results of a petrologic and geochemical study, *J. Geophys. Res.*, *104*, 22,859–22,883.

Veirs, S. R., R. E. McDuff, M. D. Lilley, and J. R. Delaney (1999), Locating hydrothermal vents by detecting buoyant, advected plumes, *J. Geophys. Res.*, *104*, 29,239–29,247.

Von Damm, K. L. (2000), Chemistry of hydrothermal vent fluids from 9°–10°N, East Pacific Rise: "Time zero," the immediate posteruptive period, *J. Geophys. Res.*, *105*, 11,203–11,222.

Weekly, R. T., M. Tolstoy, F. Waldhauser, D. R. Bohnenstiehl, and W. Kim (2005), Increasing seismic activity at 9°50′N on the East Pacific Rise RIDGE 2000 Integrated Studies Site from October 2003 through April 2004, *Eos Trans. AGU*, *86*(52), Fall Meet. Suppl., Abstract T31A–0495.

White, D. J., and R. M. Clowes (1990), Shallow crustal structure beneath the Juan de Fuca Ridge from 2-D seismic refraction tomography, *Geophys. J. Int.*, *100*, 349–367.

White, S. N., S. E. Humphris, and M. C. Kleinrock (1998), New observations on the distribution of past and present hydrothermal activity in the TAG area of the Mid-Atlantic Ridge, *Mar. Geophys. Res.*, *20*, 41–56, doi:10.1023/A:1004376229719.

Wilcock, W. S. D., and J. R. Delaney (1996), Mid-ocean ridge sulfide deposits: Evidence for heat extraction from magma chambers or cracking fronts?, *Earth Planet. Sci. Lett.*, *145*, 49–64.

Wilcock, W. S. D., S. D. Archer, and G. M. Purdy (2002), Microearthquakes on the Endeavour Segment of the Juan de Fuca Ridge, *J. Geophys. Res.*, *107*(B12), 2336, doi:10.1029/2001JB000505.

Wilcock, W. S., et al. (2004), Local earthquakes on the Endeavour Segment of the Juan de Fuca Ridge: First seismic results from the Keck seismic/hydrothermal observatory, *Eos Trans. AGU*, *85*(47), Fall Meet. Suppl., Abstract B13A–0180.

Wilson, D. S. (1993), Confidence intervals for motion and deformation of the Juan de Fuca Plate, *J. Geophys. Res.*, *98*, 16,053–16,071.

Yoerger, D. R., D. S. Kelley, and J. R. Delaney (2000), Fine-scale three-dimensional mapping of a deep-sea hydrothermal vent site using the Jason ROV system, *Int. J. Robotics Res.*, *19*, 1000–1014.

Zelt, C. A., and R. B. Smith (1992), Seismic traveltime inversion for 2-D crustal velocity structure, *Geophys. J. Int.*, *108*, 16–34.

J. M. Babcock, A. J. Harding, and G. M. Kent, Institute of Geophysics and Planetary Physics, Scripps Institute of Oceanography, University of California, San Diego, UCSD Mail Code 0225, 9500 Gilman Drive, La Jolla, CA 92093-0225, USA. (jbabcock@ucsd.edu; aharding@ucsd.edu; gkent@ucsd.edu)

J. P. Canales, Department of Marine Geology and Geophysics, Woods Hole Oceanographic Institution, MS 24, Woods Hole, MA 02543, USA. (jpcanales@whoi.edu)

S. M. Carbotte, J. B. Diebold, and M. R. Nedimovic, Division of Marine Geology and Geophysics, Lamont-Doherty Earth Observatory, Columbia University, 61 Route 9W, P.O. Box 1000, Palisades, NY 10964-8000, USA. (carbotte@ldeo.columbia.edu; johnd@ldeo.columbia.edu; mladen@ldeo.columbia.edu)

R. S. Detrick, Department of Marine Geology and Geophysics, Woods Hole Oceanographic Institution, MS 37, Woods Hole, MA 02543, USA. (rdetrick@whoi.edu)

E. M. Van Ark, MIT-WHOI Joint Program in Marine Geology and Geophysics, 77 Massachusetts Ave. 54-526, Cambridge, MA 02139, USA. (emilyva@mit.edu)

W. S. D. Wilcock, School of Oceanography, University of Washington, Seattle, WA 98195-7940, USA. (wilcock@ocean.washington.edu)